

## Few-electron quantum dots

L P Kouwenhoven<sup>1</sup>, D G Austing<sup>2</sup> and S Tarucha<sup>2,3</sup>

<sup>1</sup> Department of Applied Physics, DIMES and ERATO Mesoscopic Correlation Project, Delft University of Technology, PO Box 5046, 2600 GA Delft, The Netherlands

<sup>2</sup> NTT Basic Research Laboratories, Atsugi-shi, Kanagawa 243-0129, Japan

<sup>3</sup> ERATO Mesoscopic Correlation Project, University of Tokyo, Bunkyo-ku, Tokyo 113-0033, Japan

Received 3 January 2001, in final form 3 April 2001

### Abstract

We review some electron transport experiments on few-electron, vertical quantum dot devices. The measurement of current versus source–drain voltage and gate voltage is used as a spectroscopic tool to investigate the energy characteristics of interacting electrons confined to a small region in a semiconducting material. Three energy scales are distinguished: the single-particle states, which are discrete due to the confinement involved; the direct Coulomb interaction between electron charges on the dot; and the exchange interaction between electrons with parallel spins. To disentangle these energies, a magnetic field is used to reorganize the occupation of electrons over the single-particle states and to induce changes in the spin states. We discuss the interactions between small numbers of electrons (between 1 and 20) using the simplest possible models. Nevertheless, these models consistently describe a large set of experiments. Some of the observations resemble similar phenomena in atomic physics, such as shell structure and periodic table characteristics, Hund’s rule, and spin singlet and triplet states. The experimental control, however, is much larger than for atoms: with one device all the artificial elements can be studied by adding electrons to the quantum dot when changing the gate voltage.

(Some figures in this article are in colour only in the electronic version; see [www.iop.org](http://www.iop.org))

**Contents**

	Page
1. Introduction	703
2. Device parameters and experimental setup	707
3. Theory	709
3.1. Constant-interaction model	709
3.2. Single-particle states in a two-dimensional harmonic oscillator	711
4. Magnetic-field dependence of the ground states	713
4.1. Shell filling and Fock–Darwin states	713
4.2. Hund’s rule and exchange energy	717
5. Excitation spectrum	719
5.1. Coulomb diamonds	719
5.2. Excitation stripes	722
6. Limitations of the constant-interaction model	724
7. Singlet–triplet transition for $N = 2$	726
8. Experimental determination of direct Coulomb and exchange interactions	728
9. Conclusions	734
Acknowledgments	735
References	735

## 1. Introduction

Quantum dots are small man-made structures in a solid, typically with sizes ranging from nanometres to a few microns. They consist of  $10^3$ – $10^9$  atoms with an equivalent number of electrons. In semiconductors all electrons are tightly bound to the nuclei except for a small fraction of free electrons. This small number can be anything from a single, free electron to a puddle of several thousands in quantum dots defined in a semiconductor. Current nanofabrication technology allows us to precisely control the size and shape of these dots. The electronic properties of dots show many parallels with those of atoms. Most notably, the confinement of the electrons in all three spatial directions results in a quantized energy spectrum. Quantum dots are therefore regarded as *artificial atoms* [1]. Since we are interested in electronic transport, we limit this review to quantum dots that are fabricated between the source and drain electrical contacts. In such a setup, current–voltage measurements are used to observe the atom-like properties of the quantum dot. In addition, it is possible to vary the exact number of electrons on the dot by changing the voltage applied to a nearby gate electrode. This control allows one to scan through the entire periodic table of artificial elements by simply changing the voltage.

The symmetry of a quantum system is responsible for degeneracies in the energy spectrum. The three-dimensional spherically symmetric potential around atoms yields degeneracies known as the shells, 1s, 2s, 2p, 3s, 3p, . . . . The electronic configuration is particularly stable when these shells are completely filled with electrons, occurring at the atomic numbers of 2, 10, 18, 36, . . . . These are the magic numbers of a three-dimensional spherically symmetric potential. Up to atomic number 23 the atomic shells are filled sequentially by electrons in a simple manner (i.e. mixing between levels originating from different shells starts at atomic number 24). Within a shell, Hund's rule determines whether a spin-down or a spin-up electron is added [2].

The confinement potential of dots can, to some extent, be chosen at will. Figure 1(c) shows examples of different shapes that can be fabricated. Here, we will mainly consider the circular pillar, which has the highest degree of symmetry. The quantum dot is inside the pillar and has the shape of a two-dimensional disc [3,4]. The repulsive, confinement potential is rather soft and can be approximated by a harmonic potential. (This  $r^2$ -dependence, instead of the  $1/r$  attractive potential in atoms, has several consequences for the energy spectrum and relaxation times [5].) The symmetry of such a two-dimensional cylindrically symmetric, harmonic potential leads to a two-dimensional shell structure with the magic numbers 2, 6, 12, 20, . . . . Note that the lower degree of symmetry in two-dimensional structures leads to a lower magic number sequence.

In this review we concentrate on the electronic transport properties of few-electron quantum dot devices which contain circular symmetry. In particular, we discuss a coherent set of experiments performed at NTT and Delft University. Many other electron transport experiments have been performed on planar or lateral devices defined in two-dimensional electron gases of semiconductor heterostructures [1, 6]. ([6] also reviews the history of the early developments in this field, something that we omit here.) In those devices the electron number is usually unknown and symmetry is absent. On the other hand, those devices are more flexible for integration in small quantum circuits and for addressing them by radio-frequency and microwave signals. The absence of symmetry has also been turned into an advantage by using them for extensive studies on chaos in quantum systems [7]. Besides semiconductor devices, metallic grains [8] and molecular devices [9] have also exhibited a discrete energy spectrum in electron transport. For all these experiments we refer to the existing reviews [1,6,9] and their references.

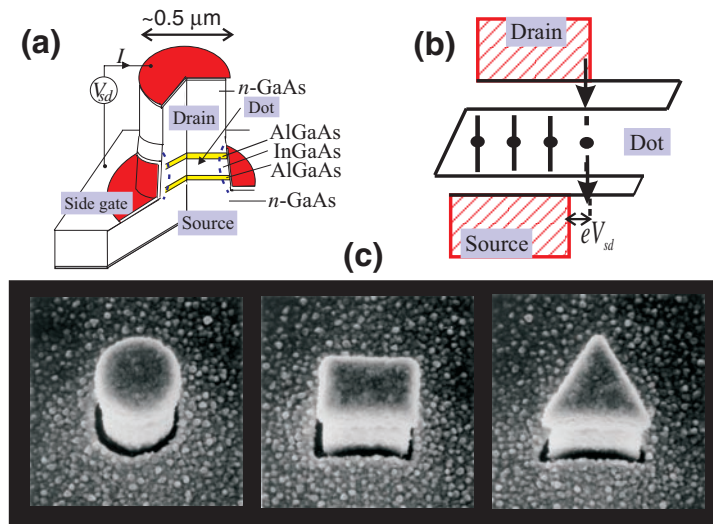


**Figure 1.** (a) Schematic diagram of a semiconductor heterostructure. The dot is located between the two AlGaAs tunnel barriers. A negative voltage applied to the side gate squeezes the dot thus reducing the effective diameter of the dot (dashed curves). (b) Corresponding energy diagram. In this case electrons can tunnel from occupied states in the drain via the dot to an empty state in the source. The source–drain voltage,  $V_{sd}$ , determines the difference in the Fermi energies between the two electrodes. The current is blocked when this energy window lies in-between two states in the dot. (c) Scanning electron micrographs of quantum dot pillars with various shapes. The pillars have widths of about  $0.5 \mu\text{m}$ .

Before describing specific experiments, we first introduce the central ideas related to atomic-like properties and explain how these are observed in *single-electron transport*. Electron tunnelling from the source to dot and from dot to the drain is dominated by an essentially classical effect that arises from the discrete nature of charge. When relatively high-potential barriers separate the dot from the source and drain contacts, tunnelling to and from the dot is weak and the number of electrons on the dot,  $N$ , will be a well defined integer. A current flowing via a sequence of tunnelling events of single electrons through the dot requires this number to fluctuate by one. The Coulomb repulsion between electrons on the dot, however, results in a considerable energy cost for adding an extra electron charge. Extra energy is therefore needed, and no current will flow until increasing the voltage provides this energy. This phenomenon is known as *Coulomb blockade* [10]. To see how this works in practice, we consider the schematic pillar structure in figure 1(a). The quantum dot is located in the centre of the pillar and can hold up to  $\sim 100$  electrons. The diameter of the dot is a few hundred nanometres and its thickness is about 10 nm. The dot is sandwiched between two non-conducting barrier layers, which separate it from conducting material above and below, i.e. the source and drain contacts. A negative voltage applied to a metal gate around the pillar squeezes the diameter of the dot's lateral potential. This reduces the number of electrons, one by one, until the dot is completely empty.

Due to the Coulomb blockade, the current can flow only when electrons in the electrodes have sufficient energy to occupy the lowest possible energy state for  $N + 1$  electrons on the dot (figure 1(b)). By changing the gate voltage, the ladder of the dot states is shifted through the Fermi energies of the electrodes. This leads to a series of sharp peaks in the measured current (figure 2(a)). At any given peak, the number of electrons alternates between  $N$  and

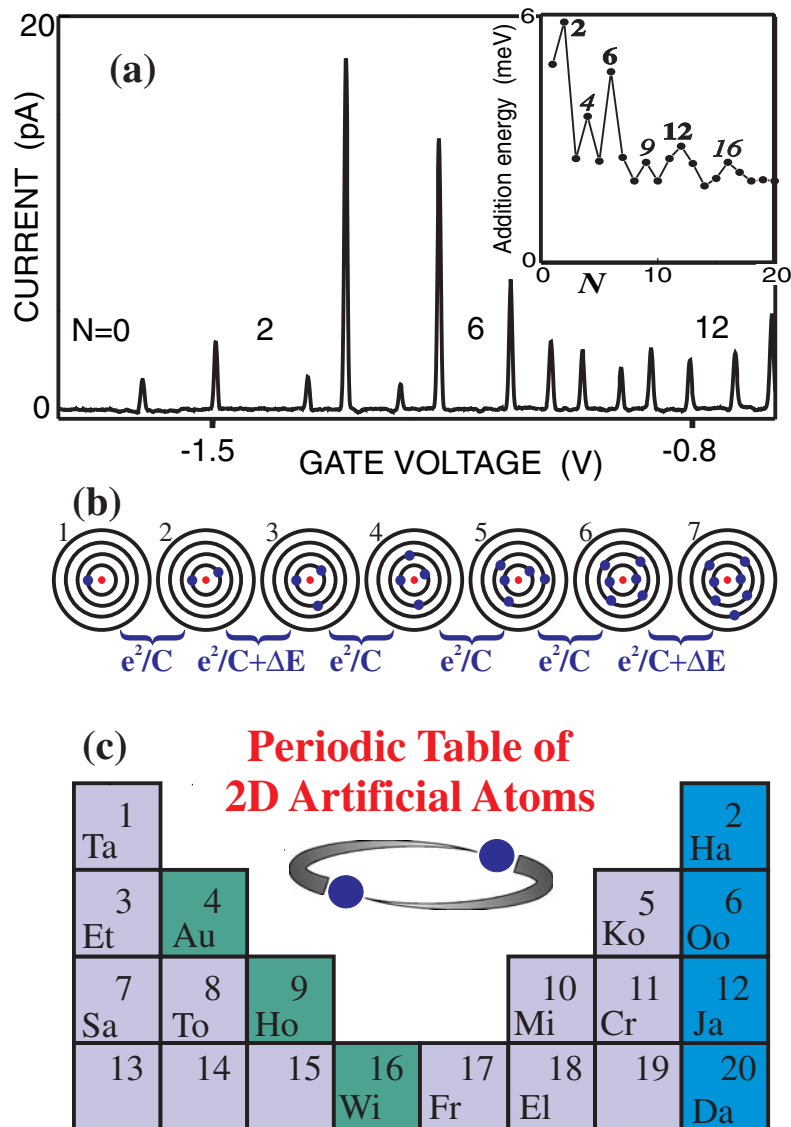


**Figure 2.** Current flowing through a two-dimensional circular quantum dot on varying the gate voltage. (a) The first peak marks the voltage where the first electron enters the dot, and the number of electrons,  $N$ , increases by one at each subsequent peak. The distance between adjacent peaks corresponds to the addition energies (see inset). (b) The addition of electrons to circular orbits is shown schematically. The first shell can hold two electrons whereas the second shell can contain up to four electrons. It therefore costs extra energy to add the third and seventh electron. (c) The electronic properties following from a two-dimensional shell structure can be summarized in a periodic table for two-dimensional elements. (The elements are named after team members from NTT and Delft.)

$N + 1$ . Between the peaks, the Coulomb blockade keeps  $N$  fixed and no current can flow. The distance between consecutive peaks is proportional to the so-called *addition energy*,  $E_{\text{add}}$ , which is the energy difference between the transition points of ( $N$  to  $N+1$ ) and ( $N + 1$  to

$N + 2$ ) electrons. Compared to atomic energy, the addition energy for a dot is equal to the difference between the ionization energy and the electron affinity [11]. The simplest model for describing the energetics is the *constant-interaction (CI) model* [6, 10], which crudely assumes that the Coulomb interaction between the electrons is independent of  $N$ . In this model, the addition energy is given by  $E_{\text{add}} = e^2/C + \Delta E$ , where  $\Delta E$  is the energy difference between consecutive quantum states. The Coulomb interactions are represented as a charging energy,  $e^2/C$ , of a single electron charge,  $e$ , on a capacitor  $C$ .

Despite its simplicity, this model is remarkably successful in providing an elementary understanding. The first peak in figure 2(a) marks the energy at which the first electron enters the dot, the second records the entry of the second electron and so on. The spacing between peaks, measured in gate voltage, is directly proportional to the addition energy. Note that the spacing is not constant and significantly more energy is needed to add an electron to a dot with 2, 6 and 12 electrons (inset figure 2(a)), i.e. the first few magic numbers for a two-dimensional circular harmonic potential.

Figure 2(b) shows the two-dimensional orbits allowed in the dot. The orbit with the smallest radius corresponds to the lowest energy state. This state has zero angular momentum and, as the s-states in atoms, can hold up to two electrons with opposite spin. The addition of the second electron thus only costs the charging energy,  $e^2/C$ . Extra energy,  $\Delta E$ , is needed to add the third electron since this electron must go into the next energy state. Electrons in this orbit have an angular momentum  $\pm 1$  and two spin states so that this second shell can contain four electrons. The sixth electron fills up this shell so that extra energy is again needed to add the seventh electron.

In atomic physics, Hund's rule states that a shell is first filled with electrons with parallel spins until the shell is half full. After that filling continues with anti-parallel spins. In the case of two-dimensional artificial atoms, the second shell is half filled when  $N = 4$ . This maximum spin state is reflected by a somewhat enhanced peak spacing, or addition energy (inset to figure 2(a)). Half filling of the third and fourth shells occur for  $N = 9$  and 16. These phenomena can be summarized in a periodic table for two-dimensional elements (figure 2(c)). The rows are shorter than those for three-dimensional atoms due to the lower degree of symmetry.

Quantum dots have been shown to provide a two-dimensional analogy for real atoms. Due to their larger dimensions, dots are suitable for experiments that cannot be carried out in atomic physics. It is especially interesting to observe the effect of a magnetic field,  $B$ , on the atom-like properties. A magnetic flux-quantum in an atom typically requires a  $B$ -field as high as  $10^6$  T, whereas for dots this is of order 1 T. (A flux quantum is  $h/e = BA$ , where  $A$  is the area of the dot.) The scale of a flux-quantum corresponds to a considerable change in the shape of the orbits. The change in orbital energy is roughly  $\hbar eB/m^*$ , which is as much as  $1.76 \text{ meV T}^{-1}$  in GaAs due to the small effective mass  $m^* = 0.067m_e$ . A magnetic field has, on the other hand, a negligible effect on the Zeeman spin splitting,  $g\mu_B B$ , which is only  $\sim 0.025 \text{ meV T}^{-1}$  in GaAs, since  $g_{\text{GaAs}} = -0.44$ . A magnetic field therefore is about 70 times more effective for changing the orbital energy than for changing the Zeeman spin splitting in GaAs. We will thus neglect Zeeman spin splitting throughout this review. However, the spin does play an important role via Hund's rule. The associated energy is the exchange energy between electrons with parallel spins. In section 4.2, we extend the so-called CI model to include Hund's rule. This model, which treats the quantum states, the direct Coulomb interaction and the exchange interaction separately provides a good introduction to the physics of interacting particles. When we understand the interactions between a small number of electrons we can gradually increase  $N$  and see how many-body interactions arise.

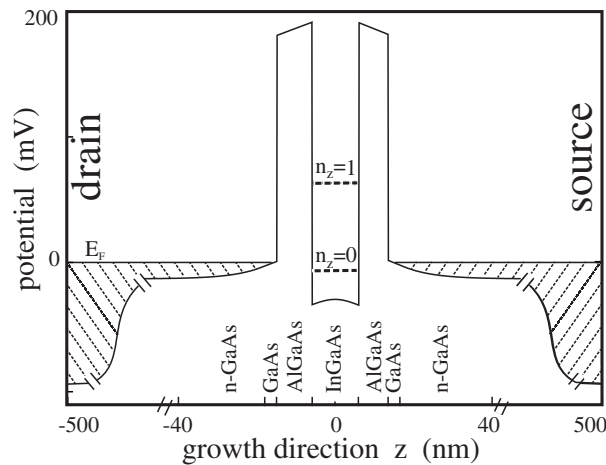


**Figure 3.** Self-consistent calculation of the energy diagram of the unpatterned double-barrier heterostructure from which the pillars are fabricated [14]. The electron density in the contacts gradually increases moving away from the tunnel barriers, which can be seen from the increasing distance between the Fermi energy and the conduction band edge. The structure is designed such that the lowest quantum state in the vertical  $z$ -direction is partially occupied and the second state always stays empty.

## 2. Device parameters and experimental setup

The pillars in figure 1(c) are in fact three-terminal field-effect transistors. The current through the transistor can be switched from on to off by changing the gate voltage. In this type of transistor there is not just one threshold voltage but a quasi-periodic set of voltages where the current switches. Only a small fraction of a single-electron charge is sufficient to drive the switch. That is why these devices are named *single-electron transistors*, or *SETs*. It is as yet unclear whether SETs will have a commercial impact in future electronics [12].

Our quantum dot SET is a miniaturized resonant tunnelling diode [13]. The pillars are etched from a semiconductor double-barrier heterostructure and a metal gate electrode is deposited around the pillar. The surface potential together with the gate potential confines the electrons in the lateral  $x$ - and  $y$ -directions while the double-barrier structure provides confinement in the vertical  $z$ -direction (figure 1(a)). The dot is formed in the central well that is made of undoped  $\text{In}_{0.05}\text{Ga}_{0.95}\text{As}$  and has a thickness of 12.0 nm. Undoped  $\text{Al}_{0.22}\text{Ga}_{0.78}\text{As}$  layers form the tunnel barriers. The upper barrier has a thickness of 9.0 and the lower barrier is 7.5 nm thick. The conducting source and drain contacts are made from Si-doped n-GaAs. The concentration of the Si dopants increases away from the two barriers. It is zero up to 3 nm and then increases stepwise from  $0.75 \times 10^{17}$  to  $2.0 \times 10^{18} \text{ cm}^{-3}$  at 400 nm away from the barriers. This variation in material and doping leads to the conduction band profile shown in figure 3 [14].

A key ingredient of this heterostructure is the inclusion of 5% indium in the well. This lowers the bottom of the conduction band in the well to 32 meV below the Fermi level of the contacts. From the confinement potential in the vertical,  $z$ -direction it follows that the lowest quantum state in the well is 26 meV above the bottom of the conduction band. This state is thus 6 meV below the Fermi level of the contacts. (The well can in good approximation be regarded as a two-dimensional system since the second quantum state in the  $z$ -direction is 63 meV above the Fermi level. These states are never occupied in the

present experiments.) To reach equilibrium, the well is filled with electrons until the highest occupied state in the dot is as close to as possible, but lower than the Fermi levels in the contacts. The key feature of this vertical quantum dot system is that it contains electrons without applying voltages. This allows one to study the linear transport regime; i.e. the current in response to a very small source–drain voltage,  $V_{sd}$ . In contrast, in previously studied structures, GaAs without indium was used as the well material [15, 16]. The lowest state in the well is then above the Fermi level of the contacts. It is then necessary to apply a large  $V_{sd}$  to force electrons into the well and to obtain a current flow. From these materials two-terminal [15] as well as three-terminal devices [16] have been fabricated. Other techniques, where the barriers are doped with Si, have been successful in accumulating electrons in the well [17, 18]. The nearby presence of charged donors, however, has the disadvantage of introducing strong disorder in the dot. By optimizing the doping profile and using capacitance spectroscopy, Ashoori *et al* [19] succeeded in measuring the linear response of few-electron dots. These measurements have shown several features that are similar to those discussed in this review.

The fabrication of the gate around the pillar starts with the definition of a metal circle with diameter  $D$  that will later serve as the top contact. This metal circle is also used as a mask for dry etching followed by wet etching to a point just below the region of the double barriers. Due to this etching combination, the top metal circle is a bit wider than the body of the pillar, as can be seen in figure 1(c). The larger top metal circle thus serves as a shadow mask for the evaporation of the metal gate; only the lower part of the pillar and the surrounding etched semiconductor are covered [3]. When the pillar's diameter  $D \approx 0.5 \mu\text{m}$ , the number of electrons is about 80 at zero gate voltage. Upon application of a negative gate voltage,  $V_g$ , the electron number,  $N$ , decreases one-by-one. At a pinch-off voltage around  $V_g \approx -1.5 \text{ V}$ ,  $N$  becomes 0. For larger negative voltages ( $V_g < \sim -2 \text{ V}$ ) a leakage current starts to flow between the gate and the source contact, inhibiting proper operation. It is therefore important to choose the material parameters properly. The pinch-off voltage is directly related to the two-dimensional electron density,  $n_e$ , in the well of the unpatterned material. Shubnikov–de Haas measurements on large area devices give  $n_e = 1.7 \times 10^{15} \text{ m}^{-2}$ . This is in good agreement with self-consistent calculations that give  $n_e = 1.67 \times 10^{15} \text{ m}^{-2}$ . From the electron density multiplied by the area we estimate that about 10 electrons are in the dot when the effective diameter  $d_{\text{eff}} = 100 \text{ nm}$ . At  $V_g = 0$  where  $N \approx 80$  the effective diameter is  $\sim 300 \text{ nm}$ , which is considerably smaller than the pillar's diameter.

It is important to realize that the geometry of these vertical dot devices leads to strong screening of the Coulomb interactions by the free electrons in the source and drain. These are only  $\sim 10 \text{ nm}$  away, which is much less than the dot's diameter. Rather than an unscreened  $1/r$ -Coulomb potential, the Coulomb interaction between two electrons at opposite edges on the dot is exponentially screened. (Note that screening occurs via positive image charges in the source generating negative image charges in the drain contacts, and vice versa. This results in nearly exponential screening.) This is illustrated when we compare the self-capacitance of a free disc with the parallel plate capacitors between the dot and contacts. The self-capacitance of a disc with diameter  $d_{\text{eff}} = 100 \text{ nm}$  is  $C_{\text{self}} = 4\epsilon_r\epsilon_0 d_{\text{eff}} \approx 50 \text{ aF}$  ( $\epsilon_r = 12.7$  in GaAs), giving a measure for the unscreened interactions by the charging energy,  $e^2/C_{\text{self}} \approx 4 \text{ meV}$ . The capacitance of a vertical dot is more realistically approximated by two parallel capacitors between the dot and the source and drain leads,  $C = C_s + C_d = \epsilon_r\epsilon_0\pi d_{\text{eff}}^2/(2d) \approx 200 \text{ aF}$ . Here,  $d = 10 \text{ nm}$  is the thickness of the tunnel barriers. The charging energy for screened interactions gives  $e^2/C \approx 1 \text{ meV}$ ; a value four times smaller than for the unscreened case. Electrons on the dot will thus have a short-range interaction. The strength of this interaction is further weakened by the finite thickness of the disc.

An important parameter in classifying the importance of electron–electron interactions is the ratio between the charging energy and the confinement energy. To estimate the confinement energy we take a harmonic potential with oscillator frequency  $\omega_0$ . We make the estimate for  $N \sim 10$  electrons corresponding to a partially filled third shell. By equating the energy at the classical turning point to the energy of the third shell ( $1/2m^*\omega_0^2d_{\text{eff}}^2/4 = 3\hbar\omega_0$ ), we obtain  $\hbar\omega_0 = 3$  meV. This implies that the separation of the single-particle states, i.e. the eigenstates of non-interacting electrons, is of the same order or even larger than the charging energy. This puts vertical dots in a very different regime compared to lateral quantum dots where the separation between single-particle states is typically 5–10 times smaller than the charging energy [6].

The measurements in this review are performed at a temperature of 100–200 mK. Below 500 mK the temperature has little effect. Above that, the Coulomb peaks start to broaden and the peak heights decrease. The measurement circuit is shown schematically in figure 1(a). The current,  $I$ , flows vertically through the dot in response to a dc voltage,  $V_{\text{sd}}$ , applied between the source and drain contacts. To measure the ground state (GS) energies, a sufficiently small voltage is applied to give a linear-response regime. A typical value is  $V_{\text{sd}} = 100$   $\mu\text{V}$ . The gate voltage,  $V_{\text{g}}$ , is typically varied between  $-2.5$  and  $+0.7$  V. Beyond these values leakage occurs through the Schottky barrier between the gate and the source. A magnetic field can be applied up to 16 T, directed parallel to the current.

One aspect worth noting about the pillar devices is that the measurements generally reproduce in great detail. In all the more or less 20 devices measured with  $D$  between 0.4 and 0.54  $\mu\text{m}$ , large addition energies are found for  $N = 2$  and 6. In about 10 of these a large addition energy is also observed for  $N = 12$ . Hund’s rule states are often observed for  $N = 4$ , and 9, and sometimes also for  $N = 16$ . Traces like the one shown in figure 2(a) reproduce in detail, even after we cycle the device several times to room temperature. (To be precise, the peak spacings and heights reproduce in detail, but not the precise gate voltages where the peaks occur.) This degree of reproducibility, which is on the level with single-particle states, is unprecedented in solid-state devices.

### 3. Theory

#### 3.1. Constant-interaction model

In this section we introduce the CI model that provides an approximate description of the electronic states of quantum dots [6, 10, 20]. The CI model is based on two important assumptions. First, the Coulomb interactions of an electron on the dot with all other electrons, in and outside the dot, are parametrized by a constant capacitance  $C$ . Second, the discrete, single-particle energy spectrum, calculated for non-interacting electrons, is unaffected by the interactions. The CI model approximates the total GS energy,  $U(N)$ , of an  $N$  electron dot by

$$U(N) = [e(N - N_0) - C_{\text{g}}V_{\text{g}}]^2/2C + \sum_N E_{n,l}(B) \quad (1)$$

where  $N = N_0$  for  $V_{\text{g}} = 0$ . The term  $C_{\text{g}}V_{\text{g}}$  is a continuous variable and represents the charge that is induced on the dot by the gate voltage,  $V_{\text{g}}$ , through the gate capacitance,  $C_{\text{g}}$ . The total capacitance between the dot and the source, drain and gate is  $C = C_{\text{s}} + C_{\text{d}} + C_{\text{g}}$ . The last term of equation (1) is a sum over the occupied states,  $E_{n,l}(B)$ , which are the solutions to the single-particle Schrödinger equation described in the next section. Note that only these single-particle states depend on the magnetic field.

The electrochemical potential of the dot is defined as  $\mu_{\text{dot}}(N) \equiv U(N) - U(N - 1)$ . Electrons can flow from left to right when  $\mu_{\text{dot}}$  is between the potentials,  $\mu_{\text{left}}$  and  $\mu_{\text{right}}$ , of the

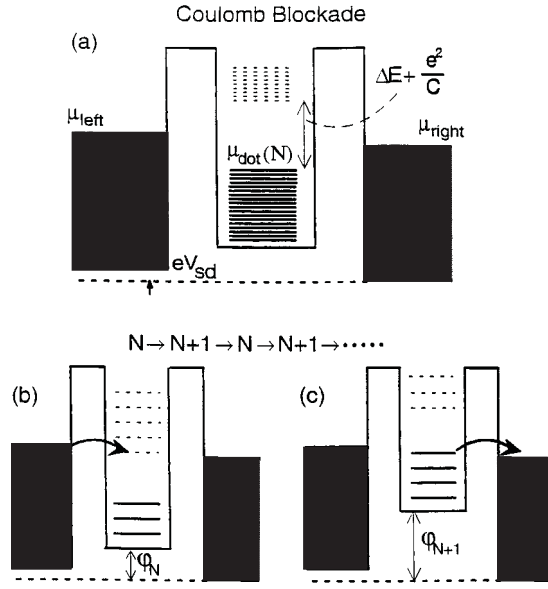


**Figure 4.** Potential landscape through a quantum dot. The states in the contacts are filled up to the electrochemical potentials  $\mu_{\text{left}}$  and  $\mu_{\text{right}}$ , which are related by the external voltage  $V_{\text{sd}} = (\mu_{\text{left}} - \mu_{\text{right}})/e$ . The discrete single-particle states in the dot are filled with  $N$  electrons up to  $\mu_{\text{dot}}(N)$ . The addition of one electron to the dot raises  $\mu_{\text{dot}}(N)$  (i.e. the highest solid curve) to  $\mu_{\text{dot}}(N+1)$  (i.e. the lowest dashed curve). In (a) this addition is blocked at low temperatures. In (b) and (c) the addition is allowed since here  $\mu_{\text{dot}}(N+1)$  is aligned with the reservoir potentials  $\mu_{\text{left}}$  and  $\mu_{\text{right}}$  by means of the gate voltage. (b) and (c) show two parts of the sequential tunnelling process at the same gate voltage. (b) shows the situation with  $N$  and (c) with  $N+1$  electrons on the dots.

leads (with  $eV_{\text{sd}} = \mu_{\text{left}} - \mu_{\text{right}}$ ), i.e.  $\mu_{\text{left}} > \mu_{\text{dot}}(N) > \mu_{\text{right}}$  (figure 4). For small voltages,  $V_{\text{sd}} \approx 0$ , the  $N$ th Coulomb peak is a direct measure of the lowest possible energy state of an  $N$ -electron dot, i.e. the GS electrochemical potential  $\mu_{\text{dot}}(N)$ . From equation (1) we obtain

$$\mu_{\text{dot}}(N) = (N - N_0 - 1/2)E_c - e(C_g/C)V_g + E_N. \quad (2)$$

The addition energy is given by

$$\begin{aligned} \Delta\mu(N) &= \mu_{\text{dot}}(N+1) - \mu_{\text{dot}}(N) = U(N+1) - 2U(N) + U(N-1) \\ &= E_c + E_{N+1} - E_N = e^2/C + \Delta E, \end{aligned} \quad (3)$$

with  $E_N$  being the topmost filled single-particle state for an  $N$  electron dot. The related atomic energies are defined as  $A = U(N) - U(N+1)$  for the electron affinity and  $I = U(N-1) - U(N)$  for the ionization energy [11]. Their relation to the addition energy is  $\Delta\mu(N) = I - A$ .

The electrochemical potential is changed linearly by the gate voltage with the proportionality factor  $\alpha = (C_g/C)$  (equation (2)). The  $\alpha$ -factor also relates the peak spacing in the gate voltage to the addition energy:  $\Delta\mu(N) = e\alpha(V_g^{N+1} - V_g^N)$  where  $V_g^N$  and  $V_g^{N+1}$  are the gate voltages of the  $N$ th and  $(N+1)$ th Coulomb peaks, respectively.

### 3.2. Single-particle states in a two-dimensional harmonic oscillator

For the simplest explanation of the ‘magic numbers’ we ignore, for the moment, Coulomb interactions between the electrons on the dot. The familiar spectrum of a one-dimensional

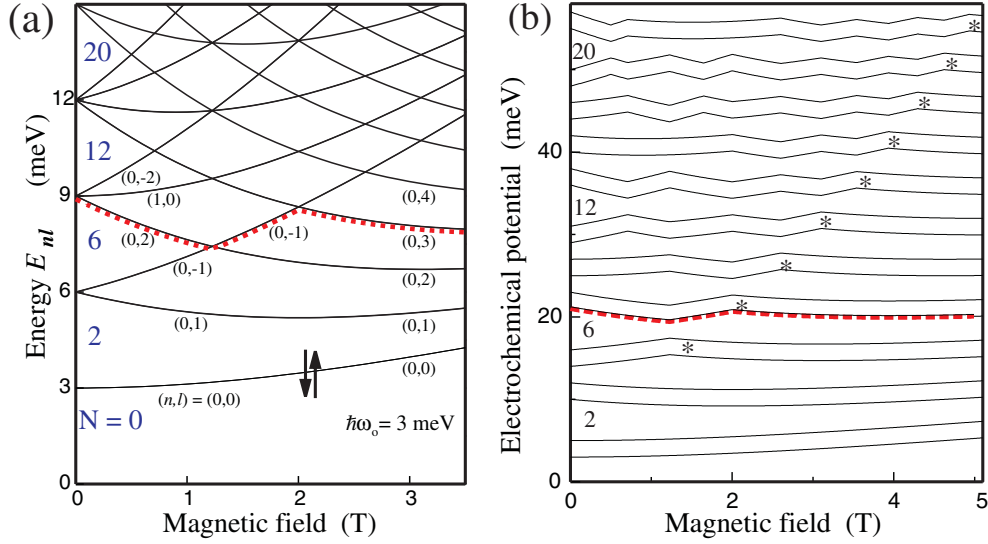


**Figure 5.** (a) Calculated single-particle states versus magnetic field, known as the Fock–Darwin spectrum, for a parabolic potential with  $\hbar\omega_0 = 3$  meV. Each orbital state is two-fold spin-degenerate. The dashed curve highlights the transitions that the seventh and eighth electrons make as  $B$  is increased. (b) The Fock–Darwin spectrum transferred into electrochemical potential curves using equation (2). Traces for a particular  $N$  are taken from (a) and subsequent traces are separated by a fixed charging energy,  $E_c = 2$  meV, as illustrated by the dashed curve for  $N = 7$ . The electrochemical potentials for electron pairs (i.e.  $N = \text{odd}$  and  $(N + 1) = \text{even}$ ) have the same  $B$ -dependence and are separated by  $E_c$  over the entire  $B$  range.

harmonic oscillator  $E_n = (n + 1/2)\hbar\omega$  becomes  $E_{n,l} = (2n + |l| + 1)\hbar\omega_0$  in two dimensions. Here,  $n (= 0, 1, 2, \dots)$  is the radial quantum number, and  $l (= 0, \pm 1, \pm 2, \dots)$  is the angular momentum quantum number of the oscillator and  $\omega_0$  is the oscillator frequency.

The eigenenergies,  $E_{n,l}$ , as a function of  $B$  can be solved analytically for a two-dimensional parabolic confining potential  $V(r) = 1/2m^*\omega_0^2 r^2$  leading to a spectrum known as the Fock–Darwin states [21]

$$E_{n,l} = (2n + |l| + 1)\hbar(\omega_0^2 + 1/4\omega_c^2)^{1/2} - 1/2l\hbar\omega_0 \quad (4)$$

where  $\hbar\omega_0$  is the electrostatic confinement energy and  $\hbar\omega_c = \hbar eB/m^*$  is the cyclotron energy (for GaAs  $\hbar\omega_c = 1.76$  meV at 1 T). Each state  $E_{n,l}$  is two-fold spin-degenerate.

Figure 5(a) shows  $E_{n,l}$  versus  $B$  for a typical value  $\hbar\omega_0 = 3$  meV. The orbital degeneracies at  $B = 0$  are lifted in a magnetic field. For instance, as  $B$  is increased from 0 T, a single-particle state with a positive or negative angular momentum,  $l$ , shifts to lower or higher energy, respectively. The lowest energy state  $(n, l) = (0, 0)$  is a two-fold spin degenerate (the Zeeman spin-splitting in a magnetic field is neglected). The next state has a double orbital degeneracy,  $E_{0,1} = E_{0,-1}$ . This degeneracy forms the second shell, which can contain up to four electrons when we include the two-fold spin degeneracy. It will be filled for  $N = 6$ . The third shell has a triple-orbital degeneracy formed by  $(1, 0)$ ,  $(0, 2)$  and  $(0, -2)$  so that it can hold up to six electrons. This shell leads to the magic number  $N = 12$ . We note that the degeneracy of the  $(1, 0)$  state with the  $(0, 2)$  and  $(0, -2)$  states is specific for a parabolic confinement; a non-parabolic component lifts this degeneracy [22].

When the magnetic field is increased the electron occupying the highest energy state is forced into different orbital states. These transitions are indicated in figure 5(a) by a dashed

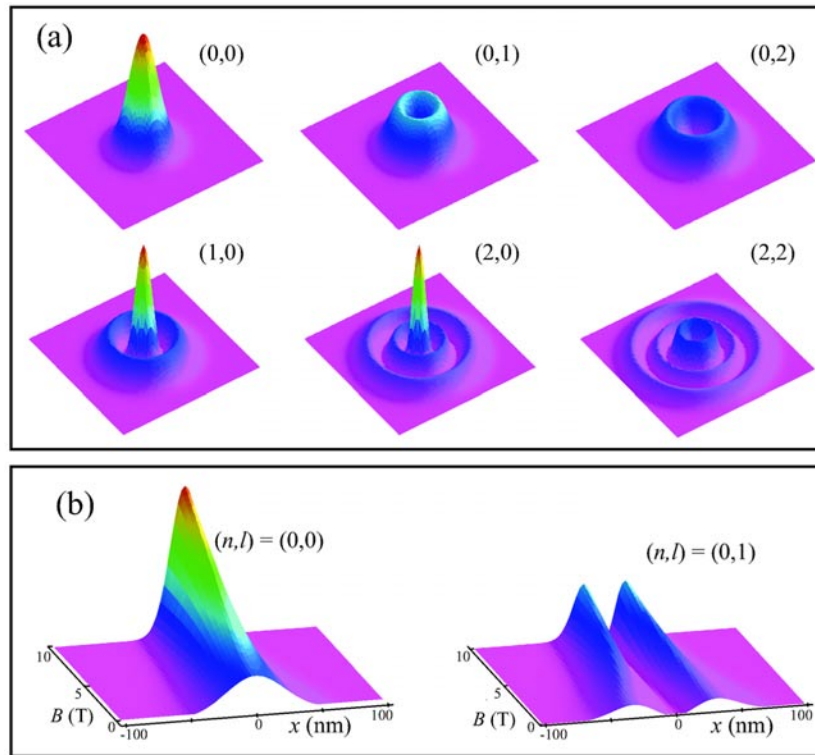


**Figure 6.** (a) Examples of the square of the single-particle wavefunctions for the Fock–Darwin states for different quantum numbers  $(n, l)$ .  $n$  sets the number of nodes in the radial direction whereas  $l$  determines the size of the dip in the centre and the radial extent of the wavefunction. (b) Magnetic-field dependence for two squared wavefunctions (i.e. the s and p states) taking  $\hbar\omega_0 = 3$  meV. The typical width decreases considerably when  $B$  is increased to 10 T. (This is also reflected in the increased height since the area below the curve stays constant.)

curve for the case of seven non-interacting electrons on the dot. At low  $B$ , the highest occupied state is  $(0, 2)$ , which decreases in energy with  $B$ . At some point it crosses the increasing energy state  $(0, -1)$ . For a potential  $\hbar\omega_0 = 3$  meV this occurs at 1.3 T. The seventh electron makes a second transition into the state  $(0, 3)$  at 2 T. Similar transitions are also seen for other  $N$  with an increasing number of crossings for larger  $N$ . After the last crossing the electrons occupy states forming the so-called, lowest orbital Landau level. These states are characterized by the quantum numbers  $(0, l)$  with  $l \geq 0$ . Including spin-degeneracy, this last crossing is denoted as a filling factor of 2, in analogy to the quantum Hall effect in a large two-dimensional electron gas. In contrast to the bulk two-dimensional case, the confinement lifts the degeneracy in this Landau level. The calculated separations between single-particle states at, for example,  $B = 3$  T, is still quite large (between 1 and 1.5 meV in figure 5(a)). The sequence of magic numbers in the lowest Landau level is simply 2, 4, 6, 8, . . . . We again note that for similar crossings between orbital states in real atoms, magnetic fields of the order of  $10^6$  T are required.

In the CI model a Coulomb charging energy is added to the non-interacting Fock–Darwin states to include, in a simple way, electron–electron interactions. The addition spectrum then follows from the electrochemical potential  $\mu_{\text{dot}}(N)$  (equation (2)) where the topmost filled state  $E_N$  in figure 5(a) is added to the charging contributions. The  $B$ -field evolution of  $\mu_{\text{dot}}(N)$  is

shown in figure 5(b). Note that spin-degenerate states appear twice with a separation equal to  $E_c$ . The magic numbers 2, 6, 12, 20, . . . are visible as enhanced spacings near  $B = 0$ , which are equal to  $E_c + \hbar\omega_0$ . An even–odd parity effect is seen in the lowest Landau level (beyond the labels \*), where the energy separations for  $N = \text{even}$  are larger than those for  $N = \text{odd}$ .

For some applications it is helpful to know the wavefunctions belonging to the Fock–Darwin eigenenergies

$$\psi_{n,l}(r, \phi) = \frac{e^{il\phi}}{\sqrt{2\pi}l_B} \sqrt{\frac{n!}{(n+|l|)!}} e^{-r^2/4l_B^2} \left(\frac{r}{\sqrt{2}l_B}\right)^{|l|} L_n^{|l|} \left(\frac{r^2}{2l_B^2}\right) \quad (5)$$

where  $l_B = (\hbar/m^*\Omega)^{1/2}$  is the characteristic length with  $\Omega = (\omega_0^2 + 1/4\omega_c^2)^{1/2}$  and  $L_n^{|l|}$  are generalized Laguerre polynomials. The square of the wavefunction,  $|\psi_{n,l}(r, \phi)|^2$ , is plotted in figure 6(a) for different quantum numbers  $(n, l)$ . Note that two wavefunctions with quantum numbers  $(n, \pm l)$  differ only by the phase factor  $e^{\pm il\phi}$ . The number of nodes of the wavefunction going out from the centre is given by the radial quantum number  $n$ . If the angular momentum is non-zero, then an additional node appears at  $r = 0$ . The larger  $|l|$  the wider the dip around  $r = 0$ .

When a magnetic field is applied, the characteristic length  $l_B$  decreases, indicating that the confinement becomes stronger for larger  $B$ . This is also observed as a shrinking of the wavefunctions (figure 6(b)). The effect is that when  $B$  is increased, two electrons occupying the same state will be pushed closer together. The decreasing distance between the electrons will increase the Coulomb interactions implying that the CI model will fail over these large field scales (e.g.  $\sim 10$  T). We discuss this further in the section on singlet–triplet (ST) transitions.

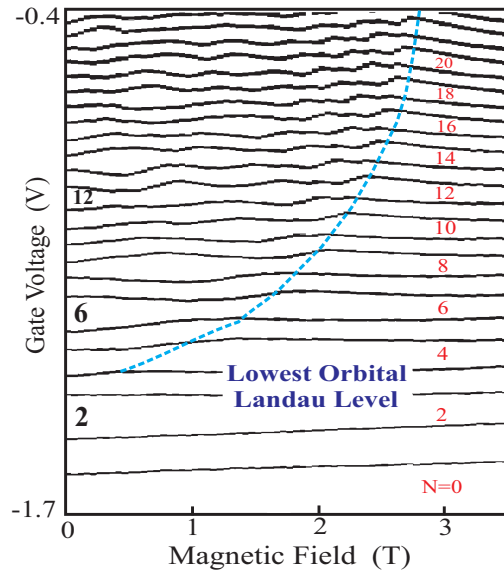
## 4. Magnetic-field dependence of the ground states

### 4.1. Shell filling and Fock–Darwin states

Figure 7 shows the measured  $B$ -dependence of the positions of the current peaks for  $N = 1$  to 24. It is constructed from many  $I-V_g$  curves, as in figure 8(a), for  $B$  increasing from 0 to 3.5 T in steps of 0.05 T. These measurements should be compared to the theoretical curve given in figure 5(b). The anomalously large peak spacings for the magic numbers  $N = 2, 6,$  and  $12$  are clearly visible near  $B = 0$ . As a function of a magnetic field the peak positions oscillate up and down a number of times. The number of these ‘wiggles’ increases with  $N$ . For each peak with  $N = \text{odd}$ , the next peak, that is for  $N + 1 = \text{even}$ , wiggles approximately in-phase. This pairing implies that the  $N$ th and  $(N + 1)$ th electrons occupy the same single-particle state with opposite spin.

The wiggling stops for  $B$  values larger than the dashed curve. This is the regime of the lowest Landau level. Close inspection shows that the peak spacing alternates here between ‘large’ for even  $N$  and ‘small’ for odd  $N$ . This is particularly clear when the peak spacings are converted to addition energies, as shown in figure 8(b). The clearly observed even–odd parity at 3 T demonstrates that in this region of the magnetic field the single-particle states are filled with two electrons with anti-parallel spins. The amplitude of the even–odd oscillations is a good measure of the separation between the single-particle states,  $\Delta E$ . For  $B = 3$  T,  $\Delta E$  decreases from  $\sim 1$  to  $\sim 0.5$  meV when  $N$  is increased to 40. This may be expected since  $N$  is increased by increasing the effective width,  $d_{\text{eff}}$ . This lowers the confinement potential that in turn leads to a reduction in  $\Delta E$ .

This trend is also seen in the  $B$ -dependence of the last wiggle (i.e. filling factor 2), as indicated in figure 7 by the dashed curve. For a fixed dot area it is expected that the occurrence of a filling factor of 2 increases linearly in  $B$  for larger  $N$  (see the  $B$ -trend of the \*-labels in



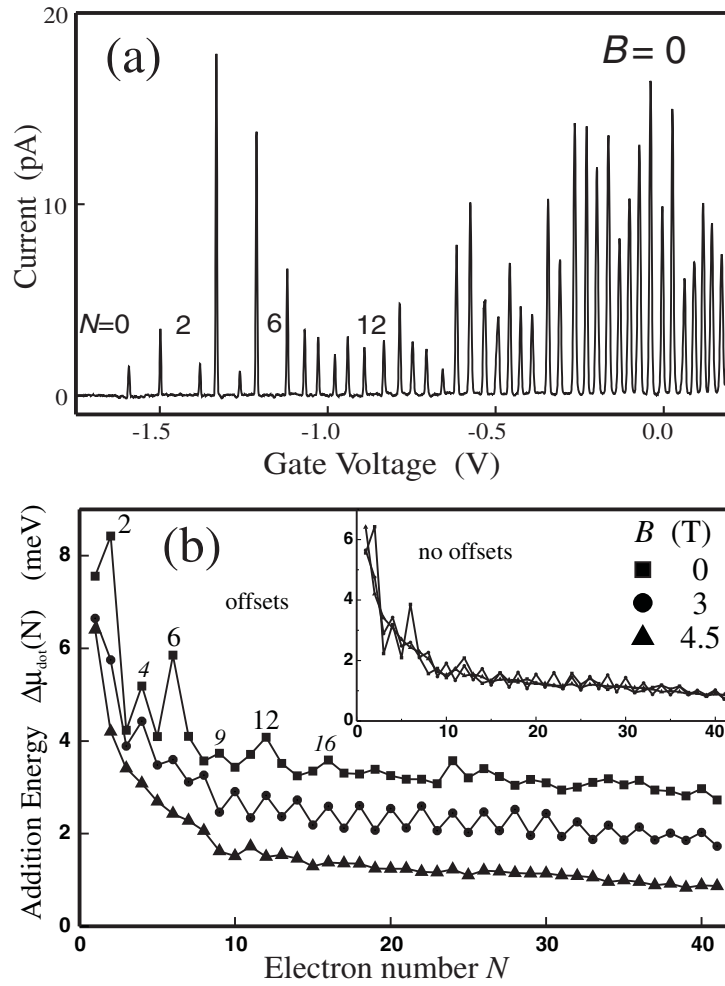
**Figure 7.** Evolution of the GS electrochemical potentials,  $\mu_{\text{dot}}(N)$ , versus  $B$ , measured on a circular quantum dot. The traces for increasing  $N$  are the positions in the gate voltage of the Coulomb peaks. Many  $I-V_g$  traces as in figure 8(a) are taken at increasing  $B$ . The magic numbers, 2, 6, 12, ... are clearly visible for the low fields. Around 3 T an even-odd parity is seen with alternating smaller and larger peak spacings.

figure 5(b)). The measured dashed curve in figure 7, however, tends to become independent of  $B$ , implying that for  $N > \sim 30$ , the gate voltage increases  $N$  by increasing the area while keeping the electron density constant. For these larger electron numbers the confinement potential is no longer parabolic. It will be flat in the middle and roughly parabolic at the dot's boundary.

At 4.5 T the addition spectrum has become a smooth curve (figure 8(b)), suggesting that alternating spin filling no longer occurs at this  $B$ -value. The inset to figure 8(b) shows that on average the  $N$ -dependence of the addition energy does not change with the magnetic field. The decreasing trend as  $N$  increases indicates a smoothly increasing capacitance, in accordance with the previous conclusion on the increasing dot area with the gate voltage. Note that these observations indicate the limited validity of the CI model (where  $C$  is assumed to be independent of  $N$ ).

Nevertheless, the CI model is particularly useful for analysing the filling of the single-particle states over a small range of electron number. A clear example is shown in figure 9, which focuses on  $N = 4-7$  symmetrically measured from  $-5$  to 5 T. The calculated addition spectrum, corresponding to figure 9(a), is shown in figure 9(b). It is clear that the fifth and sixth electrons form a pair and occupy the same single-particle state with opposite spins. At 1.3 T the evolution of the sixth peak has a maximum whereas the evolution of the seventh peak has a minimum. This corresponds to the crossing of the energy states  $(0, -1)$  and  $(0, 2)$  at 1.3 T in the Fock-Darwin spectrum of figure 5(a). The magnetic field value at this crossing is linked to a confinement potential of  $\hbar\omega_0 = 3$  meV which provides a rough estimate for the effective diameter,  $d_{\text{eff}} \approx 100$  nm for  $N \approx 6$ .

The agreement between the measured data and the results of the CI model is really striking. It clearly shows that, for low electron numbers, the occupied energy states are very well



**Figure 8.** (a)  $I-V_g$  at  $B = 0$  for  $N$  from 0 to 41. (b) Addition energies,  $\Delta\mu_{\text{dot}}(N)$ , obtained from measured peak spacings which are converted to energy using appropriate  $\alpha$ -factors. The offset for the trace at 3 T is 1 meV and for 0 T is 2 meV. The inset shows the same traces without offsets illustrating that on average the addition energy decreases smoothly with  $N$ , independent of  $B$ .

described by the Fock–Darwin spectrum. This identification of the quantum numbers of energy states is new for solid-state devices. A closer look at figure 9(a) shows that the peak evolutions for  $N = 5$  and 6 are not exact replicas. In particular, the expected cusp seen for  $N = 6$  is not visible for  $N = 5$ . We discuss in the next section that this deviation from the CI model is a result of the exchange interaction between electrons with parallel spins in the second shell; i.e. it is a manifestation of Hund’s rule.

#### 4.2. Hund’s rule and exchange energy

We now focus on the evolution of the peak positions near  $B = 0$  T and show that deviations from the CI model are related to Hund’s *first* rule. Figure 10(a) shows the  $B$ -dependence of the third, fourth, fifth, and sixth current peaks up to 2 T. The pairing of the third and fourth

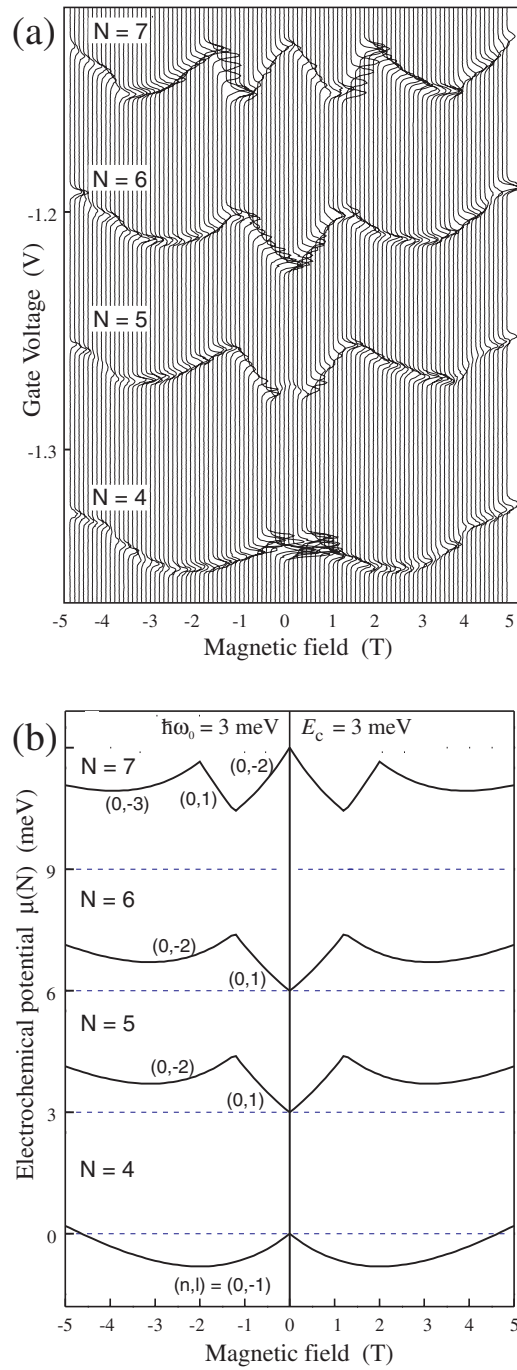


**Figure 9.** (a) GS evolution for  $N$  from 4 to 7. The individual  $I-V_g$  traces at particular values of  $B$  are still visible, including the Coulomb peaks. Note that  $B$  varies symmetrically around 0 T. The fifth and sixth electrons clearly form a pair, suggesting they always occupy the same orbital state. The cusps indicate transitions between crossing orbital states. (b) Calculated electrochemical potentials,  $\mu_{\text{dot}}(N)$ , versus  $B$  from the CI model. The comparison to the measured data in (a) clearly provides identification for the quantum numbers of the occupied single-particle states.

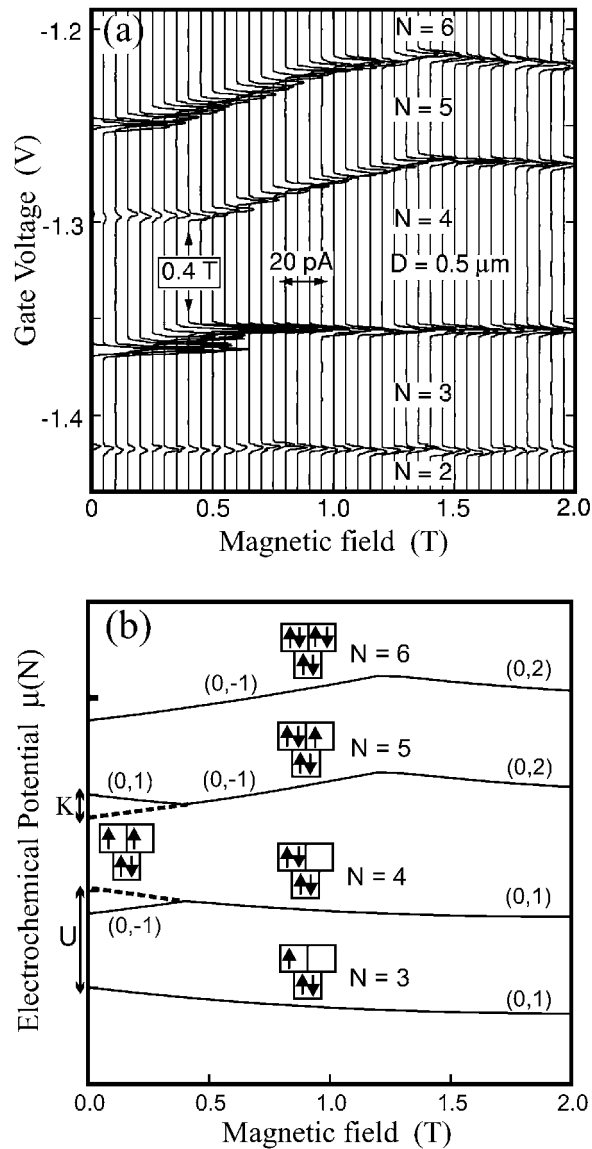


**Figure 10.** A manifestation of Hund's rule in the  $B$ -evolution of the third to sixth electron peaks from 0 to 2 T. The original data consists of  $I$ - $V_g$  traces for different  $B$ -values which are slightly offset. (b) Calculated  $B$ -evolution of the GS electrochemical potentials,  $\mu(N)$ , including an exchange interaction (solid curves) between parallel spins (see text). The two dashed curves at low  $B$  show  $\mu(N)$  without including an exchange contribution.

peaks and the fifth and sixth peaks *above* 0.4 T is clearly seen. However, *below* 0.4 T there seems to be pairing between the third and fifth peaks and the fourth and sixth peaks. This pairing is also seen in the peak heights. Apparently, a transition in pairing occurs at 0.4 T. Such extra transitions can be understood in terms of Hund's rule, which states that a shell of degenerate states will, as much as possible, be filled by electrons with parallel spins. (This is in fact Hund's *first* rule [6].)

To explain the above transitions we need to extend the CI model. If we leave out the contributions from the gate voltage one can write for the total energy  $U(N) = 1/2N(N - 1)E_c + \sum E_{n,l} - K(\sigma)$ . The last term allows us to take into account the reduction of the total energy,  $K$ , due to the exchange interaction between electrons with parallel spins. For simplicity we only take account of the exchange energy between electrons in quantum states with identical radial quantum numbers and opposite angular momentum, i.e.  $(n, \pm l)$ , and ignore all other contributions. In order to deduce the effect of the exchange energy,  $K$ , we will write out explicitly the energies  $U(N)$  and  $\mu(N)$  for  $N$  from 1 to 6. We first ignore Hund's rule and minimize the spin, i.e. the total spin  $S = 1/2$  for  $N = \text{odd}$  or  $S = 0$  for  $N = \text{even}$

$$\begin{aligned} U(1) &= E_{0,0} \\ U(2) &= E_c + 2E_{0,0} \\ U(3) &= 3E_c + 2E_{0,0} + E_{0,1} \\ U(4) &= 6E_c + 2E_{0,0} + 2E_{0,1} \\ U(5) &= 10E_c + 2E_{0,0} + 2E_{0,1} + E_{0,-1} - K \\ U(6) &= 15E_c + 2E_{0,0} + 2E_{0,1} + 2E_{0,-1} - 2K \end{aligned}$$

and

$$\begin{aligned} \mu(1) &= U(1) - 0 = E_{0,0} \\ \mu(2) &= U(2) - U(1) = E_c + E_{0,0} \\ \mu(3) &= U(3) - U(2) = 2E_c + E_{0,1} \\ \mu(4) &= U(4) - U(3) = 3E_c + E_{0,1} \\ \mu(5) &= U(5) - U(4) = 4E_c + E_{0,-1} - K \\ \mu(6) &= U(6) - U(5) = 5E_c + E_{0,-1} - K. \end{aligned}$$

According to Hund's rule the fourth electron should be added to the second shell with the same spin as the third electron (i.e.  $S = 1$ ). The third and fourth electrons then occupy the two states  $E_{0,1}$  and  $E_{0,-1}$ . We now obtain

$$U^*(4) = 6E_c + 2E_{0,0} + E_{0,1} + E_{0,-1} - K.$$

For a zero magnetic field,  $E_{0,1} = E_{0,-1}$  and thus  $U^*(4) < U(4)$  so that the GS for  $N = 4$  has  $S = 1$ . In a magnetic field the two angular momentum states are separated by  $E_{0,-1} - E_{0,1} = \hbar\omega_c$ . As long as  $\hbar\omega_c < K$  the GS remains  $S = 1$ . A transition to  $S = 0$  occurs at  $\hbar\omega_c = K$ . The experimentally observed transition at  $B = 0.4$  T yields  $K = 0.7$  meV.

Below 0.4 T not only the electrochemical potential for  $N = 4$ , but also for  $N = 5$  is affected by this extra spin transition due to Hund's rule

$$\begin{aligned} \mu^*(4) &= U^*(4) - U(3) = 3E_c + E_{0,-1} - K \\ \mu^*(5) &= U(5) - U^*(4) = 4E_c + E_{0,1}. \end{aligned}$$

Note that  $\mu^*(4)$  follows the  $B$ -dependence of  $E_{0,-1}$  implying that the fourth peak pairs with the sixth peak for  $B < 0.4$  T. Similarly, the third peak then pairs with the fifth peak. Note that the observed kink in  $N = 5$  does not correspond to a transition in the five-electron system, i.e. there is no transition in  $U(5)$ . The observed kink in  $\mu(5) = U(5) - U(4)$  is just the result of a transition in  $U(4)$ .

Figure 10(b) shows the calculated electrochemical potentials for  $\hbar\omega_c = 3$  meV,  $E_c = 3$  meV and  $K = 0.7$  meV. For  $B < 0.4$  T we plot  $\mu(3)$ ,  $\mu^*(4)$ ,  $\mu^*(5)$ , and  $\mu(6)$ . For  $B > 0.4$  T we plot  $\mu(3)$ ,  $\mu(4)$ ,  $\mu(5)$ , and  $\mu(6)$ . Remarkable agreement is found with the measured data in figure 10(a) including the pairing between the third and fifth and the fourth

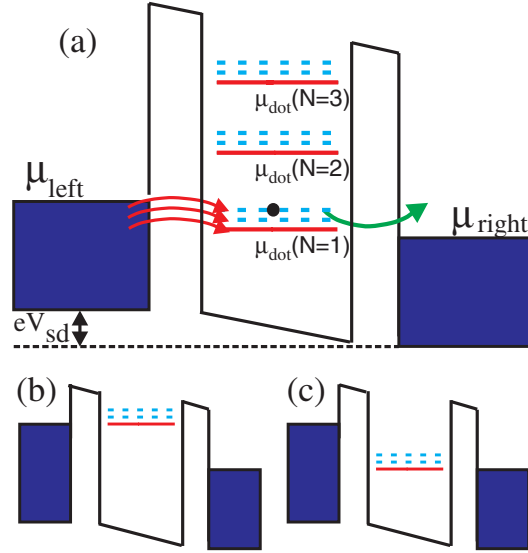


**Figure 11.** Schematic energy diagram to illustrate tunnelling via ES. The voltage between the source and drain contacts,  $V_{sd}$ , opens an energy window,  $eV_{sd} = \mu_{\text{left}} - \mu_{\text{right}}$ , between the occupied states in the left and empty states in the right electrodes. Electrons in this window can contribute to the current. (a) In this case  $eV_{sd}$  is large enough that tunnelling can occur either via the GS or one of the two ESs. (b) This alignment of states occurs at a gate voltage corresponding to the lower edge of an excitation stripe (e.g. figure 13). The alignment shown in (c) occurs at a gate voltage corresponding to the upper edge of an excitation stripe.

and sixth electrons at low  $B$ . Figure 10(b) also shows the quantum numbers  $(n, l)$  to identify the transitions in angular momentum, and illustrates the spin configurations.

At  $B = 0$  the addition energies,  $\Delta\mu(N) = \mu(N+1) - \mu(N)$ , become

$$\begin{aligned}\Delta\mu(1) &= E_c \\ \Delta\mu(2) &= E_c + E_{0,1} - E_{0,0} = E_c + \hbar\omega_o \\ \Delta\mu(3) &= E_c - K \\ \Delta\mu(4) &= E_c + K \\ \Delta\mu(5) &= E_c - K.\end{aligned}$$

The peak spacing for  $N = 2$  is enhanced due to the separation in single-particle energies. The spacing for  $N = 4$  is expected to be larger than the spacings for  $N = 3$  and 5 by twice the exchange energy  $2K (= 1.4 \text{ meV})$ . These enhancements are indeed observed in the addition curve for  $B = 0$  in figure 8(b). Similar bookkeeping also explains the enhancements for  $N = 9$  and 16 that correspond to a spin-polarized, half-filled third shell ( $S = 3/2$ ) and fourth shell ( $S = 2$ ). This simple example shows that within a shell degeneracies can be lifted due to interactions. This spin-polarized filling is completely analogous to Hund's rule in atomic physics. Although this bookkeeping method is very simple it explains various details in the data well. Self-consistent calculations of several different approaches [23] support this model of a constant charging energy with corrections that account for the exchange energies following Hund's rule.

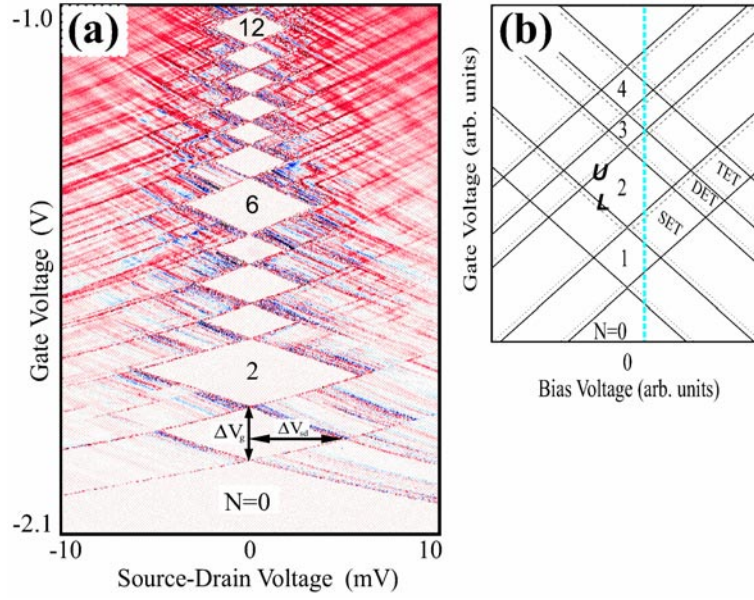


**Figure 12.** (a) Differential conductance,  $\partial I / \partial V_{sd}$ , plotted in a colour scale in the plane of  $(V_g, V_{sd})$  for  $N = 0-12$  at  $B = 0$ . The white regions (i.e. the Coulomb diamonds) correspond to  $\partial I / \partial V_{sd} \approx 0$ , red indicates a positive  $\partial I / \partial V_{sd}$ , while blue indicates some regions of negative  $\partial I / \partial V_{sd}$ . (b) Schematic stability diagram. In the diamonds at non-zero bias voltages transport can take place via single-electron tunnelling (SET), double-electron tunnelling (DET), or triple-electron tunnelling (TET). ‘U’ (‘L’) labels the upper (lower) diamond edge.

## 5. Excitation spectrum

The previous discussion concerned the GS energies of few-electron quantum dots. The experiments were all performed in linear-response regime (i.e.  $I \propto V_{sd}$ ) where  $eV_{sd} \ll \Delta E, E_c, k_B T$ . Access to higher-lying energy states is obtained when the voltage is increased so that  $eV_{sd} \sim \Delta E, E_c \gg k_B T$ . Figure 11 illustrates that increasing the voltage increases the energy window between occupied states in the left reservoir and empty states in the right reservoir. Any state lying in this window can contribute to current flow. In the situation sketched in figure 11 the first electron can tunnel into the dot to the GS (solid curves) but also to the first and second excited states (ES) (dashed curves). These extra tunnelling channels are detected as an increase in the current. We will discuss two types of such spectroscopic measurements. We discuss  $\partial I / \partial V_{sd}$  first in the plane of  $(V_g, V_{sd})$  at a fixed  $B$ -value and second in the plane  $(V_g, B)$  at a fixed  $V_{sd}$ -value.

### 5.1. Coulomb diamonds

Figure 12(a) shows the differential conductance,  $\partial I / \partial V_{sd}$ , versus  $(V_g, V_{sd})$  for  $N = 0-12$  at  $B = 0$ . Such a data set is assembled by taking a trace of  $\partial I / \partial V_{sd}$  versus  $V_{sd}$  at a fixed value for  $V_g$ . For the next trace,  $V_g$  is slightly changed and this is repeated many times (in total 555 traces each with 4000 data points). The  $\partial I / \partial V_{sd}$  recorded is then displayed in colour as a function of two variables. The light, diamond-shaped areas correspond to regions of the Coulomb blockade where  $\partial I / \partial V_{sd} \approx 0$ . Inside the diamonds the number of electrons is fixed. The size and shape of the diamonds therefore reflects the regions where the charge,  $eN$ , on

the device is stable. Figure 12(a) is often called a *stability diagram*. Note that the width of the zero-current region, labelled as  $N = 0$ , keeps increasing when we make  $V_g$  more negative. This implies that here the dot is indeed empty, which allows us to assign absolute electron numbers to the blockaded regions.

Along the  $V_{sd} \approx 0$  axis  $N$  changes to  $N + 1$  where adjacent diamonds touch. These are the linear-response Coulomb peaks as already shown in figure 2(a). The unusually large diamonds for  $N = 2, 6,$  and  $12$  demonstrate that filled shells have an anomalously high stability. Also the half-filled shells with a maximized spin, i.e. Hund's rule states for  $N = 4$  and  $9$ , appear to be more stable judging by the slightly enhanced size of the  $N = 4$  and  $9$  diamonds.

When  $V_{sd}$  is increased at a fixed gate voltage inside the  $N$  electron diamond, an extra electron can tunnel through the dot when  $V_{sd}$  reaches the edge of the diamond. The upper diamond edges corresponds to the  $N + 1$  electron GS. Here, the voltage provides the necessary energy to add an electron. ES of the  $N + 1$  electron system that enter the transport window are seen as 'lines' running parallel to the upper edges of the diamond. Similarly, the lower edges reflect the  $N - 1$  electron GS where the voltage allows for the extraction of an electron.

Figure 12(b) illustrates the different tunnelling channels in a theoretical stability diagram. The diamonds centred around  $V_{sd} \approx 0$  are the Coulomb blockade regions. In the adjacent diamonds SET takes place where the electron number fluctuates between  $N$  and  $N + 1$ . Diamonds at larger  $V_{sd}$  allow for two, three, etc electron tunnelling at the same time. Solid curves indicate GS energies where the extra electron has only access to the lowest possible energy state. The dotted curves running parallel to the upper edges of the  $N$ -electron diamonds indicate the energy of the ES of an  $N + 1$  electron system. In the CI model the energy difference between the GS and the ES is constant. The dashed curves immediately beneath the lower edge of the  $N$ th diamond indicate ES of the  $N - 1$  electron system.

Not all lines are equally visible in a measurement of the differential conductance when the two barriers have different thicknesses. The change in  $\partial I / \partial V_{sd}$  is largest when electrons first tunnel through the thickest barrier, as for instance is the case in figure 11 [6]. For this reason the curves in figure 12(a) running from the upper left to the lower right are much more visible than the curves from the lower left to the upper right.

A stability diagram allows for a straightforward determination of the conversion factor,  $\alpha$ , to relate the gate voltage scale to the electrochemical potential,  $\Delta\mu = \alpha \Delta V_g$  (see section 3.1). The two arrows in the  $N = 1$  diamond both indicate the addition energy measured in gate voltage and in energy. Their ratio provides the  $\alpha$ -factor,  $\alpha = e \Delta V_{sd} / \Delta V_g$ . Since the gate voltage changes the dot area, the  $\alpha$ -factor changes with  $N$ . We therefore determine  $\alpha$  for each  $N$  and find that, in the  $D = 0.5 \mu\text{m}$  dot,  $\alpha$  varies from 57 to 42 meV  $\text{V}^{-1}$  for  $N = 1-6$ , and then gradually decreases to 33 meV  $\text{V}^{-1}$  as  $N$  approaches 20.

## 5.2. Excitation stripes

In order to identify the quantum numbers associated with the ES it is necessary to study the magnetic-field dependence, as was shown for the GSs in section 4. Figure 13 shows the evolution of the first three Coulomb peaks with the magnetic field. The different panels show that increasing  $V_{sd}$  turns the peaks into stripes with a width almost independent of  $B$ . The stripes correspond to a cross-section along a vertical axis in figure 12 at finite  $V_{sd}$ . The larger the  $V_{sd}$ , the narrower the Coulomb-blockade regions. The stripe width on the gate-voltage scale equals  $e V_{sd} / \alpha$ . As well as showing the GS, the stripe also reveals the ES. Measurements such as those in figure 13 allow us to follow the evolution of the ES with magnetic field. The lower edge of the  $N$ th stripe (which lies between the Coulomb blockade regions for  $N - 1$  and

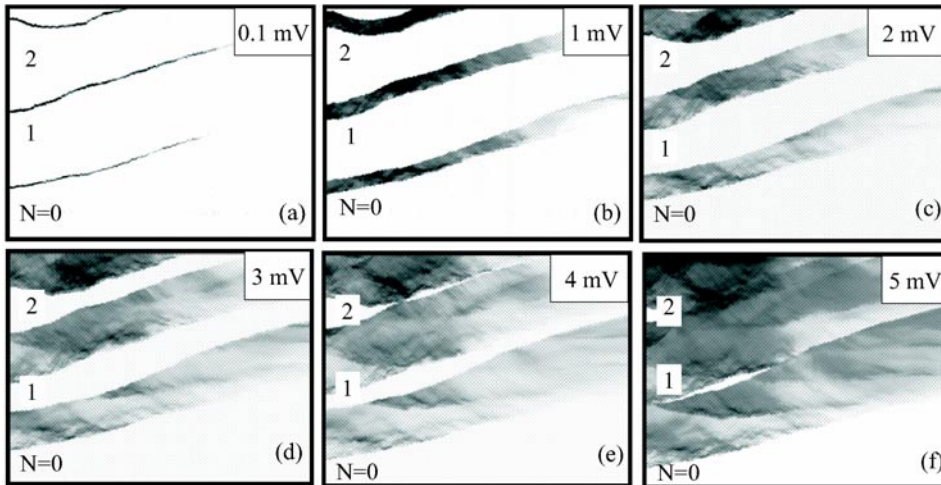


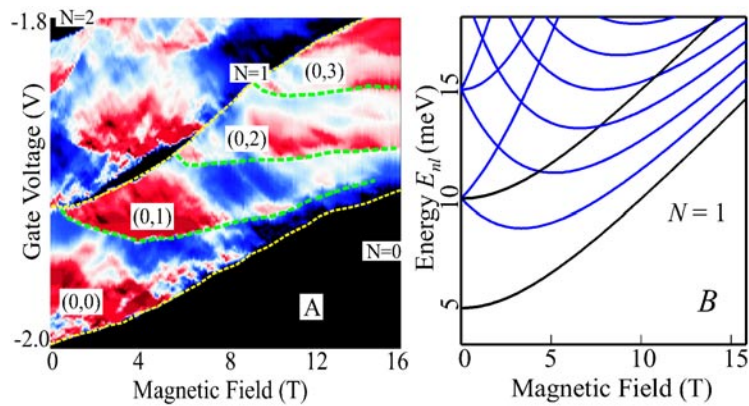
**Figure 13.**  $B$ -evolution of the current (dark regions) for different  $V_{sd}$ . In each panel  $B$  increases from 0 to 16 T from left to right. The gate voltage is varied each time over the same range on the vertical axis.

$N$  electrons) reflects the GS electrochemical potential,  $\mu_N^{GS}(B)$ . This lower edge corresponds to the situation in figure 11(b) where the  $N$ -electron GS is equal to the higher Fermi energy in the contacts. The upper edge corresponds to figure 11(c) where due to a change in the gate voltage the  $N$ -electron GS is now aligned to the lower Fermi energy and is simply a replica at  $\mu_N^{GS}(B) + eV_{sd}$ . When adjacent stripes overlap,  $eV_{sd}$  exceeds the addition energy.

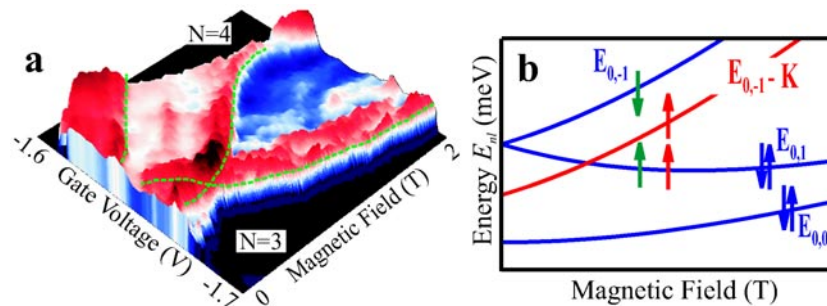
In figure 14 we focus on the first stripe taken at  $V_{sd} = 5$  mV which is equal to the  $N = 1$  addition energy (i.e. the  $N = 1$  and 2 stripes touch at  $B = 0$ ). The lower stripe edge reflects the increasing energy with  $B$  of the lowest energy state  $(n, l) = (0, 0)$  in the Fock–Darwin spectrum (see figure 14(b)). Inside the stripe a clear colour change from blue to red occurs along a continuous curve. This is an increase in current, which reflects the entry of the first ES,  $(0, 1)$ , into the energy window between the Fermi energies in the contacts. The distance to the lower stripe edge is a direct measure of the excitation energy,  $\Delta E$ , between the GS and the first ES.  $\Delta E = 5$  meV at  $B = 0$  and decreases as  $B$  increases. At higher values of  $B$  two higher-lying ESs,  $(0, 2)$  and  $(0, 3)$ , can also be distinguished although they are less clear. The comparison with the Fock–Darwin spectrum is rather good, as expected, since the one-electron system is non-interacting. From this comparison we obtain a confinement energy  $\hbar\omega_0 = 5$  meV for this gate voltage range.

Figure 15(a) shows a surface plot of the  $N = 4$  stripe measured at  $V_{sd} = 1.6$  mV. In figure 15(b) we illustrate the different possible spin configurations. Electrons  $N = 1$  and 2 always occupy the lowest energy state  $(0, 0)$  with opposite spin. Electrons  $N = 3$  and 4 together occupy the state  $(0, 1)$  for high-magnetic fields. At low-magnetic fields we have indicated the different spin configurations for  $N = 3$  and 4, which have comparable energies. (1) Opposite spins occupying  $(0, 1)$  indicated by blue arrows. The  $B$ -evolution for  $N = 4$  reflects  $E_{0,1}$ . (2) Opposite spins occupying different states,  $(0, 1)$  and  $(0, -1)$ , indicated by green arrows. Now, the  $B$ -evolution for  $N = 4$  reflects  $E_{0,-1}$ . (3) Parallel spins occupying different states,  $(0, 1)$  and  $(0, -1)$ , indicated by red arrows. The  $B$ -evolution for  $N = 4$  again reflects  $E_{0,-1}$ , but the energy is reduced by the exchange energy,  $K$ .

The measured surface plot in (a) indeed shows this  $B$ -dependence including a crossing



**Figure 14.** (a)  $I(V_g, B)$  for  $N = 1$  and  $2$  measured with  $V_{sd} = 5$  meV up to  $16$  T. The states in the  $N = 1$  stripe are indexed by the quantum numbers  $(n, l)$ . The stripe edges are highlighted by yellow dashed curves and the first three ESs by green dashed curves. (b) Calculated Fock–Darwin spectrum for  $\hbar\omega_0 = 5$  meV. The lowest black curve is the GS energy. The upper black curve is the GS energy shifted upwards by  $5$  meV. The blue states between the two thick black curves can be seen in the experimental stripe for  $N = 1$  in (a).



**Figure 15.** (a) Surface plot of the  $N = 4$  stripe measured with  $V_{sd} = 1.6$  meV up to  $2$  T. The green dashed curves highlight the  $B$ -evolution of the three lowest energy states. (b) Schematic energy diagram explaining the different possible spin configurations when there are four electrons on the dot (see text).

between the GS and first ES at  $0.4$  T. At this crossing the spins of the third and fourth electrons change from being parallel to anti-parallel. Also the second ES is seen with a  $B$ -dependence that runs roughly parallel to the first ES. The difference between these two parallel curves is a direct measure of the energy gain due to the exchange from which we extract  $K \sim 1$  meV.

### 6. Limitations of the constant-interaction model

In the previous sections we discussed the basic different methods for analysing the electronic properties of few-electron quantum dots. We would like to stress that a proper analysis is only possible by taking comprehensive data sets to build up GS and ES spectra for different electron numbers, and by applying a magnetic field to induce changes in the occupation of the states. These methods are not limited to semiconductor dots but apply equally well to other small nanostructures that are weakly coupled by tunnel barriers to electrodes. Examples where the CI model has been successfully applied include metallic grains [8] and molecules such as

carbon nanotubes [9]. The physics of the Coulomb blockade, SET and a quantized energy spectrum is therefore not limited to one particular small system, but rather provides a widely applicable framework for electron transport through nanostructures in general. The simplicity of the CI model is both the reason for its success as well for its failures. In this section we discuss in some detail these limitations.

In a non-self-consistent description that includes only first-order corrections due to the interactions between electrons, the direct Coulomb interactions,  $C_{ij}$ , between two electrons, labelled  $i$  and  $j$ , are separated from the exchange contribution,  $K_{ij}$

$$\begin{aligned} C_{ij} &= \iint |\psi_i(\mathbf{r}_1)|^2 [e^2/4\pi\epsilon_0|\mathbf{r}_1 - \mathbf{r}_2|] |\psi_j(\mathbf{r}_2)|^2 d\mathbf{r}_1 d\mathbf{r}_2 \\ K_{ij} &= - \iint \psi_i^*(\mathbf{r}_1)\psi_j(\mathbf{r}_1) [e^2/4\pi\epsilon_0|\mathbf{r}_1 - \mathbf{r}_2|] \psi_j^*(\mathbf{r}_2)\psi_i(\mathbf{r}_2) d\mathbf{r}_1 d\mathbf{r}_2. \end{aligned} \quad (6)$$

The wavefunctions,  $\psi_i$  and  $\psi_j$ , correspond to the states  $E_i$  and  $E_j$ , respectively, and  $\vec{r}_1$  and  $\vec{r}_2$  represent the positions of the two electrons. The direct Coulomb interaction,  $C_{ij}$ , acts between two charge densities. The exchange interaction,  $K_{ij}$ , also depends on the symmetry of the wavefunctions and is non-zero only for two electrons with parallel spins [2]. The simplest determination of the GS energy,  $U(N)$ , takes, for instance, Fock–Darwin wavefunctions which are the eigenfunctions for non-interacting electrons in a parabolic confinement potential. The direct Coulomb interaction and the exchange energy are then calculated using equation (6). Here, it is implicitly assumed that the interactions do not distort the wavefunctions. The interactions are thus treated as a first-order perturbation [24–27]. The CI model shares this assumption that the interactions do not mix up the single-particle states. So, in principle the CI model should only be applied in the limit where the confinement energy,  $\Delta E$ , is much larger than the interaction energies. In the few-electron vertical quantum dots this condition is partly satisfied since  $\Delta E$  is of the same order or larger than  $E_c$ . In lateral quantum dots, defined by metallic gates in a two-dimensional electron gas, one typically finds  $E_c \approx 10 \times \Delta E$  [6]. Indeed, both the self-consistent calculations [28] and the measured results [29] are found to be completely different from what is expected based on the CI model.

In a self-consistent treatment the Coulomb interactions have the effect of distorting the wavefunctions. For instance, two electrons can minimize their interaction energy by being as far apart as possible, irrespective of their single-particle wavefunctions. The eigenstates of the two-particle system then needs to be build out of many single-particle states. The execution of self-consistent calculations involves many steps of altering the wavefunctions, which in turn change the interactions, until eventually the system reaches the lowest possible energy state. Several theoretical papers have used such a scheme to calculate addition spectra for quantum dots [23, 30–36]. Note that for small electron numbers ( $N < \sim 10$ ) it is possible to numerically perform exact calculations of the eigenstates. We know of three works, Macucci *et al* [23], Zeng *et al* [24] and Wojs and Hawrlylak [37], who actually predicted a shell structure and Hund’s rule prior to the first experiment in 1996 [4].

Most theory papers treat dots as isolated discs. Screening by electrons in nearby gates or electrodes is usually ignored, although there are some exceptions [38]. In theory papers, electrons are usually added while keeping the confinement potential fixed, which is very different from changing the gate voltage. This hampers a serious comparison between theoretical and experimental results. Recent Hartree–Fock calculations by Bednarek *et al* [39], however, solved the Schrödinger equation self-consistently with a three-dimensional Poisson equation. The Poisson equation takes account of the electrostatics in the environment such as ionized donors, gate voltages, etc. The results include the self-consistent confinement potential for different gate voltages and the size and shape of the Coulomb diamonds. Since these calculations can be compared directly to our experimental data we discuss them here in some more detail.

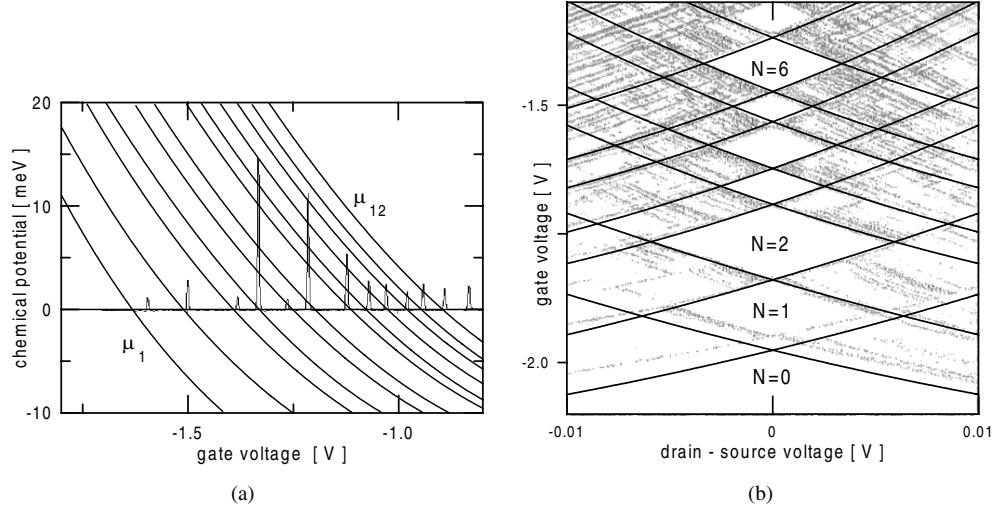


**Figure 16.** Three-dimensional self-consistent calculation for realistic device parameters. (a) Electrochemical potential (solid curves) calculated for  $N = 1, \dots, 12$  as a function of gate voltage. Zero on the vertical axis corresponds to the Fermi energies in the source and drain contacts ( $eV_{sd} = 0$ ). Coulomb peaks are expected when  $\mu_N$  crosses the Fermi energy. The measured Coulomb peaks from figure 2(a) are also shown for comparison. (b) Calculated Coulomb diamonds (solid curves) which are compared to the measured diamonds from figure 12(a). Calculations are from Bednarek *et al* [39].

The first result is that the self-consistent confinement potential is very well described by a parabola up to at least  $N \sim 12$ . For larger electron numbers the potential flattens out in the centre. This result is in accordance with the experiments, in particular with the observation of a Hund's rule state for  $N = 9$ . This maximum spin state implies that the states  $(0, \pm 2)$  are close in energy to  $(1, 0)$ . This degeneracy is specific to a parabolic potential.

Figure 16(a) shows the electrochemical potential versus gate voltage using the parameters for our devices. The crossings through zero energy identify the condition that an extra electron can be added, i.e. a peak position in the gate voltage. The calculations reproduce the experimental peak positions very well, including larger spacings for  $N = 2, 4, 6, 9$  and  $12$ . The fact that the electrochemical potential is not a linear function of the gate voltage, as assumed in equation (2), implies that the gate voltage changes the confinement strength and thereby the  $\alpha$ -factor. This non-linearity is also seen in the stability diagram in figure 16(b). Again good agreement is found in size and shape with the experimental diamonds.

## 7. Singlet-triplet transition for $N = 2$

While the CI model is very useful for small magnetic fields,  $B < \sim 1$  T, at larger  $B$  it is essential to include a varying Coulomb interaction. Here, we discuss this non-constant interaction regime for dots with one to four electrons and  $B$  between 0 and 9 T. In particular, we describe the ST transition induced by a magnetic field for a dot with two electrons.

For a two-electron dot, we only consider the two lowest single-electron states,  $E_{0,0}$  and  $E_{0,1}$ . Including the Zeeman energy, we obtain from equation (4)

$$E_{0,0} = \hbar(1/4\omega_c^2 + \omega_0^2)^{1/2} \pm 1/2g^*\mu_B B$$

$$E_{0,1} = 2\hbar(1/4\omega_c^2 + \omega_0^2)^{1/2} - 1/2\hbar\omega_c \pm 1/2g^*\mu_B B$$

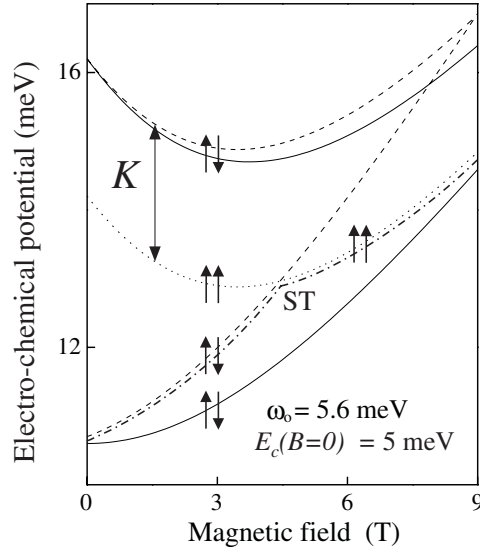


**Figure 17.** Electrochemical potential  $\mu(2)$  of a two-electron dot as a function of the magnetic field ( $\hbar\omega_0 = 5.6$  meV and  $E_c(B=0) = 5$  meV). The lower solid curve represents the GS electrochemical potential  $\mu^{\uparrow\downarrow}(2) = E_{0,0} + E_c$  (spins indicated by arrows), whereas the upper solid curve corresponds to the ES,  $\mu^{\uparrow\downarrow,ES}(2) = E_{0,1} + E_c$ . The dashed curves schematically represent the situation in which a  $B$ -dependent Coulomb interaction is taken into account. Note that the dashed curves grow faster than the solid ones. The rise of the lower one is larger due to the larger overlap of states when both electrons are in the GS. The upper dashed curve with subtraction of a constant exchange energy,  $K$ , results in the dotted curve  $\mu^{\uparrow\downarrow}(2) = E_{0,1} + E_c(B) - K$ .  $\mu^{\uparrow\downarrow}(2)$  and  $\mu^{\uparrow\downarrow}(2)$  cross at  $B \approx 4.5$  T. The GS before and after the ST transition is indicated by a dashed-dotted curve.

with  $g^*$  being the effective Landé factor and  $\mu_B$  the Bohr magneton. If we first consider non-interacting electrons we can estimate the magnetic field where the Zeeman energy induces a crossing between  $E_{0,0,\downarrow}$  (with an up-going Zeeman energy) and  $E_{0,1,\uparrow}$  (with a down-going Zeeman energy). For lower  $B$ -fields the two electrons form a singlet state,  $S = 0$ , whereas beyond this crossing the two electrons are spin-polarized and form a triplet state with  $S = 1$ . Taking typical values for  $\hbar\omega_0 = 5.6$  meV and  $g^* = -0.44$  in GaAs, we obtain this Zeeman-energy driven ST transition at  $B = 26$  T. This estimate neglects any electron–electron interactions. As we now discuss, the Coulomb interactions between the two electrons drive the ST transition towards a much lower value of  $B$ .

The interdependence of Coulomb interactions and single-particle states becomes important when a magnetic field changes the size of the electron states. For instance, the size of the Fock–Darwin states shrinks in the radial direction for increasing  $B$ . This is illustrated in figure 6(b) where cross sections of  $|\psi_{n,l}(r, \phi)|^2$  are shown versus  $B$ . When two electrons both occupy the  $E_{0,0}$  state, the average distance between them decreases with  $B$  and hence their Coulomb interaction increases. At some magnetic fields it is energetically favourable if one of the two electrons makes a transition to a state with a larger radius (i.e. from  $l = 0$  to 1), thereby increasing the average distance between the two electrons. This transition occurs when the gain in Coulomb energy exceeds the costs in single-particle energy. So, even when we neglect the Zeeman energy, the shrinking of the wavefunctions favours a transition in angular momentum.

Numerical calculations by Wagner *et al* [40] predicted these ST transitions. In our discussion here, we generalize the CI model in order to keep track of the physics that gives rise to the ST transition. In order to determine the electrochemical potentials we use a similar

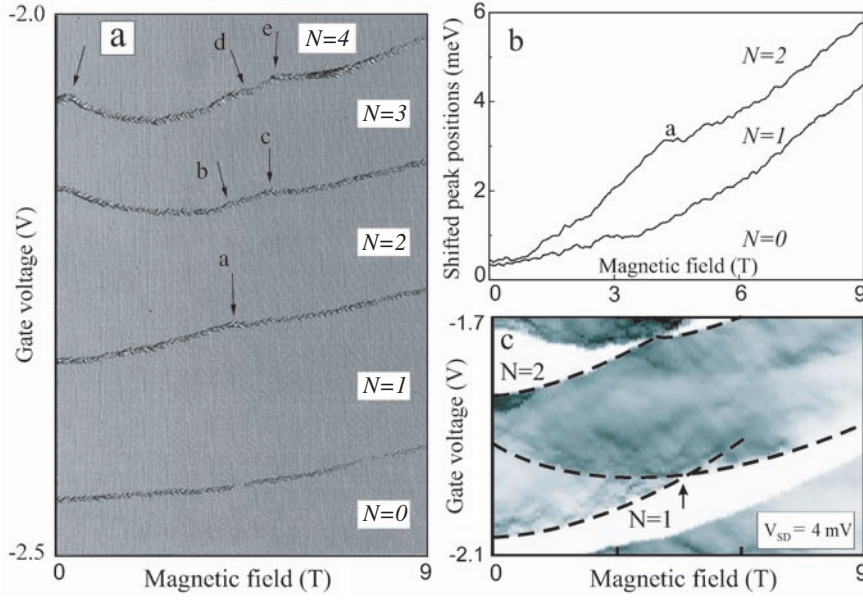


**Figure 18.** (a) Current measurement as a function of gate voltage and magnetic field (0–9 T in steps of 25 mT) for  $N = 1$ –4 and  $V_{sd} = 30 \mu\text{V}$ . The indicated transitions are discussed in the text. (b) Peak positions extracted from the data in (a) and shifted towards each other. The gate voltage is converted to electrochemical potential. (c) Grey scale plot of  $I(V_g, B)$  for  $V_{sd} = 4 \text{ mV}$ . The stripe for the second electron entering the dot is shown. The GS and first ES are accentuated by dashed curves. The crossing corresponds to the ST transition.

bookkeeping method as in section 4. With  $U^{\uparrow}(1) = E_{0,0}$  and  $U^{\uparrow\downarrow}(2) = 2E_{0,0} + E_c$  we get  $\mu^{\uparrow\downarrow}(2) = E_{0,0} + E_c$ . The first, spin-unpolarized ES is  $U^{\uparrow\downarrow, \text{ES}}(2) = E_{0,0} + E_{0,1} + E_c$  and  $\mu^{\uparrow\downarrow, \text{ES}}(2) = E_{0,1} + E_c$ . The solid curves in figure 17 show  $\mu^{\uparrow\downarrow}(2)$  and  $\mu^{\uparrow\downarrow, \text{ES}}(2)$ , where the small contribution from the Zeeman spin energy is neglected.

The next level of approximation is to include the magnetic-field dependence of the charging energy to account for the shrinking wavefunctions. The dashed curves in figure 17 rise somewhat faster than the solid curves, reflecting the  $B$ -dependence of the charging energy,  $E_c(B)$ . These dashed curves are schematic curves and do not result from any calculations.

When both electrons occupy the  $E_{0,0}$  state their spins must be anti-parallel. However, if one electron occupies  $E_{0,0}$  and the other  $E_{0,1}$ , the two electrons can also take on parallel spins; i.e. the total spin  $S = 1$ . In this case, the Coulomb interaction is reduced by the exchange energy,  $K$ , and the corresponding electrochemical potential becomes  $\mu^{\uparrow\uparrow}(2) = E_{0,1} + E_c(B) - K$ ; see the dotted curve in figure 17. Importantly,  $\mu^{\uparrow\downarrow}(2)$  and  $\mu^{\uparrow\uparrow}(2)$  cross at  $B \cong 4.5 \text{ T}$  for the parameters chosen in figure 17. So, while for  $B < 4.5 \text{ T}$  the GS energy (shown by a dashed-dotted curve) corresponds to a singlet state, for  $B > 4.5 \text{ T}$  the GS is a triplet state with total spin  $S = 1$ . Thus, while the Zeeman-driven transition would occur at 26 T, the electron–electron interactions push the ST transition down to 4.5 T. (An analogous ST transition is predicted to occur in He atoms in the vicinity of white dwarfs and pulsars at  $B = 4 \times 10^5 \text{ T}$  [41].)

Capacitance [42] and tunnelling [15] spectroscopy have provided evidence of ST transitions. Here, we review the results on our vertical circular dots [43, 44]. Figure 18 shows the linear-response Coulomb-blockade peaks for  $N = 0$ –4 reflecting the GS evolution with  $B$ . We emphasize that, based on the Fock–Darwin spectrum for non-interacting electrons,

one does not expect transitions or kinks in the  $B$ -dependence of  $\mu(N)$  for  $N = 1-4$ . The peak for  $N = 1$  indeed has a smooth  $B$ -dependence. For  $N = 2, 3$  and 4, however, we observe kinks, which are indicated by arrows. These kinks must arise from interactions not included in the CI model. (The left arrow in the  $N = 4$  trace is due to the Hund's rule state, which was discussed in section 4.2.) To focus on the difference between the  $N = 1$  and 2 traces, we have extracted the peak positions and converted their values from gate voltage to energy. The two curves in figure 18(b) are shifted towards each other and represent the variation in the electrochemical potential with  $B$ . The lowest curve for  $N = 1$  shows a smooth increase in energy in accordance with the expected trend for  $E_{0,0}$ . The  $N = 2$  trace rises faster with  $B$  than the  $N = 1$  curve. This reflects the magnetic-field dependent Coulomb interaction  $E_c(B)$ . The expected ST transition in the two-electron GS is observed as a kink labelled 'a' at 4.5 T. A crossing between the GS and the first ES is observed clearly in the corresponding excitation stripe. In figure 18(c) a grey scale plot of  $I(V_g, B)$  is shown for the  $N = 2$  stripe measured for  $V_{sd} = 4$  mV. Within the stripe, the first ES first decreases with  $B$  similar to  $\mu^{\uparrow\uparrow}(2)$  (dotted curve in figure 17). The ST crossing takes place at about 4.5 T. These measurements confirm the idea that electron-electron interactions have a strong effect on spin transitions.

We briefly discuss the  $N = 3$  and 4 curves in figure 18(a), which both contain two kinks. The left kink (labelled 'b') in  $\mu(3) = U(3) - U(2)$  is not due to a transition in the energy  $U(3)$ , but is a remnant of the two-electron ST transition in  $U(2)$ . The right kink (labelled 'c') corresponds to the transition from  $U(3) = E_{0,0}(\uparrow) + E_{0,0}(\downarrow) + E_{0,1}(\uparrow) + 3E_c$  to the spin-polarized case  $U(3) = E_{0,0}(\uparrow) + E_{0,1}(\uparrow) + E_{0,2}(\uparrow) + 3E_c$ . Detailed analysis also shows that this transition to an increasing total angular momentum and total spin is driven largely by interactions [43]. Similar transitions occur for the  $N = 4$  system where on the right of the last kink (labelled 'e') the system is again in a polarized state with sequential filling of the angular momentum states:  $U(4) = E_{0,0}(\uparrow) + E_{0,1}(\uparrow) + E_{0,2}(\uparrow) + E_{0,3}(\uparrow) + 6E_c$ .

## 8. Experimental determination of direct Coulomb and exchange interactions

We discussed in section 4.2 how Hund's rule accounts for the energy associated with spin filling near  $B = 0$ . For two electrons we have explicitly discussed how a magnetic field changes the Coulomb interactions such that the system undergoes a ST transition. In this section we discuss a simple, but general model that describes filling of two single-particle states with two interacting electrons [27]. This model that generalizes Hund's rule to arbitrary  $B$ -field [34], allows one to determine from experimental data on dots with larger electron numbers the contributions from the direct and exchange interactions (see equation (6)).

Figure 19(a) shows two, spin-degenerate single-particle states with energies  $E_a$  and  $E_b$  crossing each other at  $B = B_0$ . The GS energy,  $U(1)$ , for one electron occupying these states, equals  $E_a$  for  $B < B_0$  and  $E_b$  for  $B > B_0$  (thick curve in figure 19(a)). For two electrons we can distinguish four possible configurations with either total spin  $S = 0$  (spin-singlet) or  $S = 1$  (spin-triplet). (We neglect the Zeeman-energy difference between the  $z$ -component  $S_z = -1, 0$  and 1.) The corresponding energies,  $U_i(2, S)$  for  $i = 1-4$ , are given by

$$\begin{aligned} U_1(2, 0) &= 2E_a + C_{aa}, \\ U_2(2, 0) &= 2E_b + C_{bb}, \\ U_3(2, 1) &= E_a + E_b + C_{ab} - |K_{ab}|, \quad (\text{note } S = 1!) \\ U_4(2, 0) &= E_a + E_b + C_{ab}. \end{aligned}$$

As in equation (6),  $C_{ij}$  ( $i, j = a, b$ ) is the direct Coulomb energy between two electrons occupying states with energies  $E_i$  and  $E_j$ , and  $K_{ab}$  is the exchange energy ( $K_{ab} < 0$ ) between

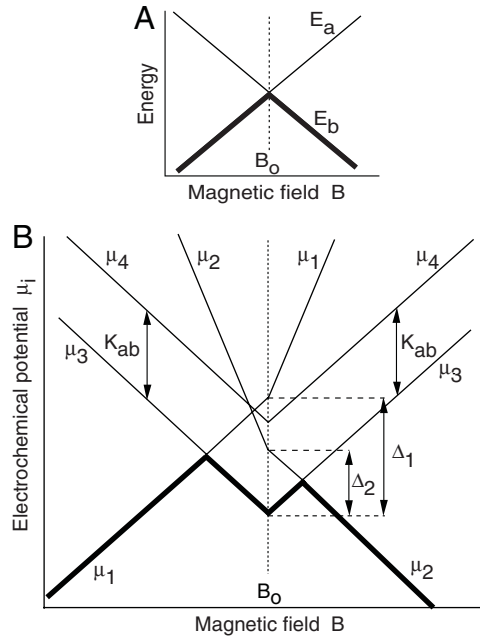


**Figure 19.** (a) Schematic diagram of two single-particle states with energies  $E_a$  and  $E_b$  crossing each other at a magnetic field  $B = B_0$ . (b) Electrochemical potential,  $\mu_i(2) = U_i(2) - U(1)$ , for two interacting electrons. The thick curve depicts the GS energy whereas the thin curves show the ES.

two electrons occupying  $E_a$  and  $E_b$  with parallel spins.

For the electrochemical potentials we obtain:  $\mu_i(2) = U_i(2) - E_a$  for  $B < B_0$  and  $\mu_i(2) = U_i(2) - E_b$  for  $B > B_0$  (see figure 19(b)). The GS has  $S = 0$  away from  $B_0$ . Near  $B_0$ , the lowest energy is  $\mu_3(2)$  for which  $S = 1$ . The downward cusp in the thick curve identifies this spin-triplet region. The transition in the GS from  $S = 0$  to 1 and then from  $S = 1$  to 0 occurs when  $\mu_1 = \mu_3$  for  $B < B_0$  and when  $\mu_2 = \mu_3$  for  $B > B_0$ . We define two energies,  $\Delta_1$  and  $\Delta_2$ , to characterize the size of the downward cusp in the GS at  $B = B_0$

$$\Delta_1 = \mu_1 - \mu_3 = C_{aa} - C_{ab} + |K_{ab}|,$$

$$\Delta_2 = \mu_2 - \mu_3 = C_{bb} - C_{ab} + |K_{ab}|$$

and

$$\Delta_1 - \Delta_2 = C_{aa} - C_{bb}.$$

Figure 20(a) shows the  $B$ -evolution of a set of Coulomb peaks for  $N = 7-16$ . The pairing between neighbouring peaks indicates anti-parallel spin filling of a single-orbital state by two electrons. Modifications to this pairing are observed for the peaks labelled by ■ at 0 T, and in each of the dashed ovals connecting pairs of peaks at a non-zero field. These are all signatures of Hund's first rule; i.e. spin-polarized filling. (Note that we will again ignore the Zeeman effect in this section.) Expansions of the evolution of the  $N = 8$  and 24 peaks clearly show the downward cusps (figure 20(b)). The dashed curves form a parallelogram, from which we obtain the energies  $\Delta_1$  and  $\Delta_2$ .

To compare the two-electron model with larger electron numbers, we assume that other states are so far away energy-wise they can be neglected. Then, the downward cusps should occur for higher *even*-electron numbers, whereas they should be absent for *odd*-electron

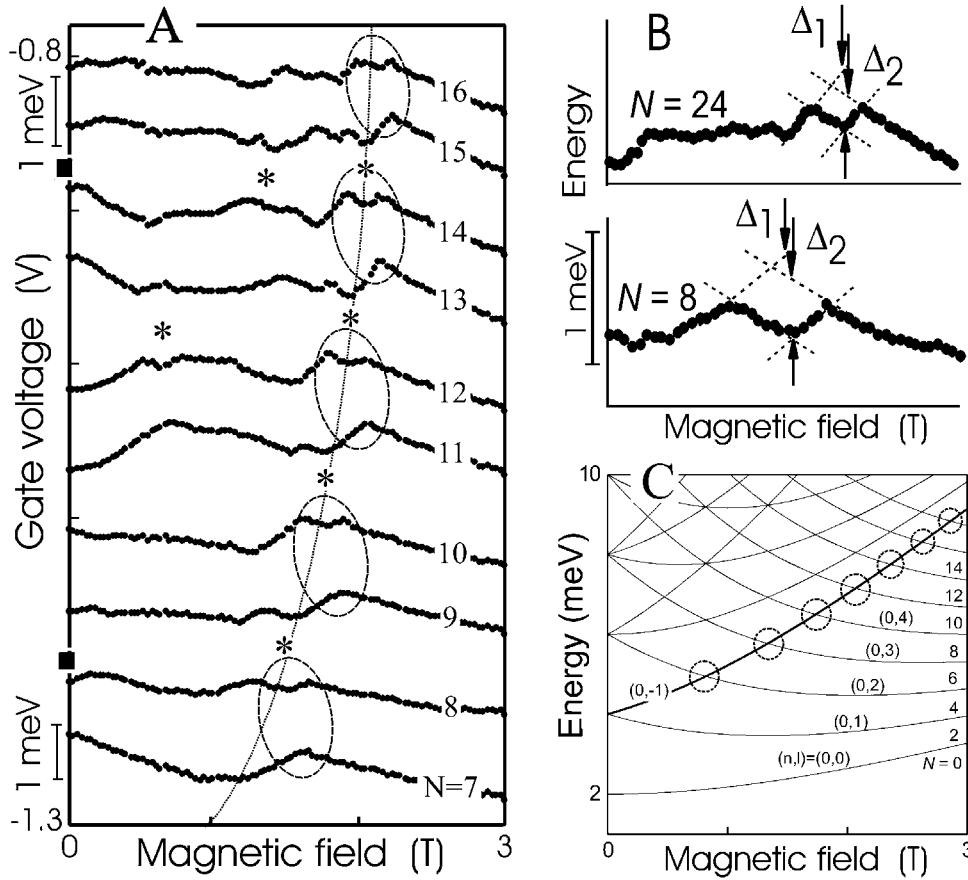


**Figure 20.** (a) Evolution of the GS energies for  $N = 7$ – $16$ . The bars along the gate voltage axis show 1 meV energy scales calibrated at  $-1.26$  and  $-0.85$  V. The dotted curve indicates the last crossing between single-particle states. Dashed ovals correlate pairs of GSs for odd and even electron numbers. The spin transitions in the GSs are indicated by ■ at  $B = 0$  T and occur in the ovals for  $B \neq 0$  T. (b) Magnified plots of the cusps for  $N = 8$  and  $24$ . The dashed curves illustrate how the interaction-energy parameters,  $\Delta_1$  and  $\Delta_2$  are determined. (c) Fock–Darwin single-particle states calculated for  $\hbar\omega_0 = 2$  meV.

numbers. This is clearly observed in the ovals in figure 20(a). For instance, the  $B$ -field dependence of the ninth peak compares well to the thick curve in figure 19(a) and the  $B$ -field dependence of the tenth peak compares well to the thick curve in figure 19(b). Other pairs of even and odd numbered peaks show the same behaviour. This justifies our assumption of simplifying the many-electron system to just one or two electrons.

Figure 21 shows the excitation spectrum in a  $dI/dV_g$  plot, taken for  $V_{sd} = 2$  mV. As in section 5.2, this larger voltage opens a sufficiently wide transport window between the Fermi levels of the source and drain, that both the GS and first few ESs can be detected. The GS and ES for  $N = 7$ – $9$  can be assigned from the magnetic-field dependence of the dark blue curves. The solid red curves highlight the GS whereas the dashed red curves indicate the ES. The set of the GS and ES curves for  $N = 7$  shows a single crossing similar to that in figure 19(a). The spectrum for  $N = 8$  compares well to figure 19(b) and we can clearly distinguish the parallelogram formed by the GS and first ES. The downward cusp in the GS for  $N = 8$

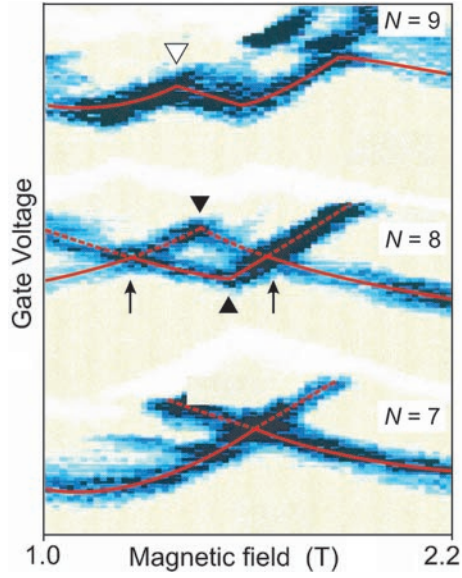


**Figure 21.**  $dI/dV_g$  in the plane of  $V_g$  and  $B$  for  $N = 7-9$  measured for  $V = 2$  mV.  $dI/dV_g > 0$  for dark blue,  $dI/dV_g < 0$  for white,  $dI/dV_g \approx 0$  for yellow. The solid red curves indicate the evolution of the GS with magnetic field whereas the dashed red curves show the ES. The two arrows indicate ST and triplet-singlet (TS) transitions in the GS for  $N = 8$ .

(labelled ▲) is at a slightly higher  $B$ -field than the upward cusp in the first ES (labelled ▼). This asymmetry implies that  $\Delta_1 > \Delta_2$ , i.e.  $C_{aa} > C_{bb}$ . The same type of asymmetry is always observed along the dashed curve in figure 20(a), implying that  $C_{aa} > C_{bb}$  for all  $N$ . Note that the GS for  $N = 9$  shows an upward cusp (labelled by ▽) quite similar in form to the first ES in the spectrum for  $N = 8$ . This implies that the filling of the ninth electron does not change the occupation configuration of the eight-electron system.

As illustrated in figure 20(b), we can derive experimental values for  $\Delta_1$  and  $\Delta_2$  for different  $N$ . These values are plotted in figure 22. We find that  $\Delta_1$  is larger than  $\Delta_2$  for all  $N$ , again implying that  $C_{aa} > C_{bb}$ . As  $N$  increases from 6 to 12,  $\Delta_1$  first increases and then slowly decreases, whilst  $\Delta_2$  slightly decreases.

To calculate direct Coulomb and exchange energies from equation (6) we take again the Fock-Darwin spectrum (figure 20(c)). We first focus on the last crossing (encircled) which always is a crossing between two states. The up-going state is always  $(n, l) = (0, -1)$ , whereas the down-going state,  $(0, l > 1)$ , has an increasing angular momentum for states with increasing energy. (The relation with figure 19 is  $E_a = E_{0,-1}$  and  $E_b = E_{0,l>1}$ .) Note that the last crossings also correspond to the dashed curve in figure 20(a).

From the Fock-Darwin wavefunctions in equation (5) and figure 6 we calculate the direct Coulomb and exchange energies for two electrons occupying two degenerate states. We take  $\hbar\omega_0 = 2$  meV and obtain values for  $\Delta_1$  and  $\Delta_2$ . The dashed curves in figure 22 show  $\Delta_1$  and  $\Delta_2$  when we neglect any screening of the interactions within the dot by electrons in the leads and in the gate. In this case the Coulomb potential falls off as  $1/r$ , where  $r$  is the distance between the electrons. For the solid curves we have approximated the screening effects by replacing the Coulomb potential by  $\exp\{-r/d\}/r$ . We have taken  $d = 10$  nm which is roughly the thickness of the tunnel barriers. Figure 22 shows that screening considerably reduces  $\Delta_1$  to values much closer to the experimental values. Screening also removes the minimum in  $\Delta_2$ ,

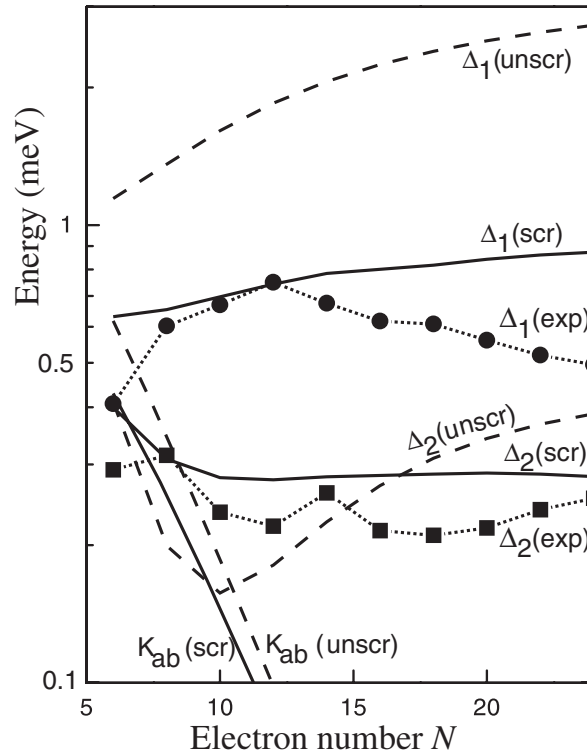


**Figure 22.** Experimental values for the energy parameters  $\Delta_1$  (●) and  $\Delta_2$  (■), on a log scale, versus electron number derived from data as shown in figure 20(a). The uncertainty in the determination of the experimental values is  $\pm 10\%$  or less. The dashed and solid curves are calculated from the Fock–Darwin wavefunctions at 2 T, for an unscreened (unscr) and screened (scr) Coulomb interaction. The calculated exchange energy  $|K_{ab}|$  between states with energies  $E_a = E_{0,-1}$  and  $E_b = E_{0,N/2-1}$  decreases quickly with  $N$ .

which is in better agreement with the experimental values.

Since the average radius of the wavefunctions increases with angular momentum, two electrons are closer together when they both occupy  $(0, -1)$  compared to both occupying  $(0, l = N/2 - 1)$  for  $l > 1$ . The direct Coulomb interactions are thus stronger in the first case. This explains our observation  $\Delta_1 > \Delta_2$ , that is  $C_{aa} > C_{bb}$  for all  $N$ . The overlap between *different* wavefunctions,  $(0, -1)$  and  $(0, l = N/2 - 1)$ , decreases with  $N$  for  $l > 1$ . This results in a decrease in both  $C_{ab}$  and  $|K_{ab}|$  with  $N$ . It then follows that  $\Delta_1$  increases until it saturates at a value equal to  $C_{aa}$ . The gradual decrease of experimental  $\Delta_1$  for  $N > 12$  is probably related to the decrease in the lateral confinement with  $N$  and thus the decrease in  $C_{aa}$ .

Note that the asymmetry ( $\Delta_1 \neq \Delta_2$ ) can only occur for  $B_0 \neq 0$ . Symmetry is required if  $B_0 = 0$ , implying that  $\Delta_1 = \Delta_2$ . Then, the eigenfunctions for the states with energy  $E_a$  and  $E_b$  must have the same spatial form, so for general reasons we conclude that at  $B_0 = 0$ :  $C_{aa} = C_{bb} = C_{ab}$  and thus  $\Delta_1 = \Delta_2 = |K_{ab}|$ . We can determine these energies for the  $N = 4, 8$  and  $14$  peaks near  $B = 0$  T (the  $N = 8$  and  $14$  peaks are labelled ■ in figure 20(a)). These peaks correspond to the GS electrochemical potentials for adding the second electron to the second, third and fourth shells, respectively. For these electron numbers we can simplify the  $N$ -electron system to a two-electron system that is well-separated in energy from the other  $N - 2$  electron system. The inset to figure 23 demonstrates the resemblance to

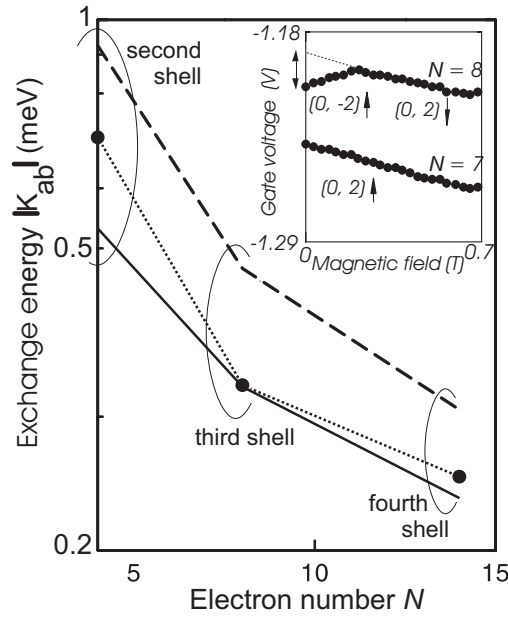


**Figure 23.** Exchange energy  $|K_{ab}|$  on a log scale associated with spin-triplets formed when each new shell is filled by just two electrons at  $B = 0$  T. The solid circles are the experimental values with a  $\sim 10\%$  uncertainty. The inset shows an expansion for the filling of the first two electrons into the third shell (i.e.  $N = 7$  and  $8$ ). The vertical double-arrow represents  $|K_{ab}|$  in units of gate voltage which is then converted into energy. The calculated curves in the main figure are for the unscreened (dashed) and screened (solid) cases.

the model of figure 19(b) for  $N = 8$  near  $B = 0$  T.

Comparing these data to the Fock–Darwin spectrum, we assign the states such that:  $E_a = E_{0,-2}$  and  $E_b = E_{0,2}$ . Likewise, for  $N = 4$  we have  $E_a = E_{0,-1}$  and  $E_b = E_{0,1}$ , and for  $N = 14$  we have  $E_a = E_{0,-3}$  and  $E_b = E_{0,3}$ . Note that these states correspond to wavefunctions with a complete overlap and since here  $\Delta_1 = \Delta_2 = |K_{ab}|$ , only exchange effects contribute to the downward cusp. The inset in figure 23 illustrates how to derive  $|K_{ab}|$ . The main figure shows that the obtained exchange energy quickly becomes smaller for the higher-lying shells. The experimental data is in good agreement with the calculations for a screened potential.

We conclude this section by noting that the two-electron model allows analysing changes in the total spin. This model is also successful for larger  $N$ -electron systems if the energies of the two topmost electrons are well separated from the other  $N - 2$  electrons. There are various calculations in the literature that support this two-electron model. These calculations use different methods such as an exact calculation for  $N < 7$  [45], Hartree–Fock calculations for  $N > 8$  [25,46], spin density-functional theory at  $B = 0$  T [35,47] and also at non-zero  $B$  [34].

## 9. Conclusions

This review has discussed the phenomena in few-electron quantum dots only for a small part of parameter space [48]. This space includes at least the following independent parameters: (1) electron number, (2) electron density, or the ratio between confinement and Coulomb energies, (3) magnetic field, and (4) tunnel coupling between dot and leads. In this concluding

section we briefly discuss the different regimes one encounters along these different axes.

- (1) *Electron number.* We have restricted this review to few-electron systems. For not too many electrons the shell structure is regularly filled with electrons obeying general rules. The total energies can be discussed by bookkeeping the different contributions. Such simple models together with numerical calculations provide a thorough understanding. In contrast, for large electron systems ( $\sim 50 < N < \sim 1000$ ) there are still many unanswered questions. In these systems there is not usually a clear separation of the energy scales [6]. The experimental status is that properties like an excitation spectrum on a particular device looks too complicated to comprehend in detail [29]. Alternatively, statistical theories have been applied to describe properties such as average energy spacings and their variance. However, this approach has also been unable to provide a consistent description of larger quantum dots [7].
- (2) *Electron density.* For a fixed electron number the density varies with the confinement potential. The two extremes on this axis are at one end a quantum regime (where confinement dominates and Coulomb interactions form a small perturbation) and at the other end a classical regime (where confinement is so weak that quantum fluctuations are absent). Our devices are somewhere in the middle. One interesting prediction is that in the classical regime the correlations due to Coulomb interactions can become so strong that the electrons freeze to regular, fixed positions and form a Wigner lattice [49]. It is unclear how such correlations can be observed unambiguously in transport experiments as in this review.
- (3) *Magnetic field.* This review covers only moderate magnetic fields, mostly for  $\omega_c < \omega_o$ . We have used the magnetic field to induce transitions between single-particle states or spin states. However, the ‘type of states’ did not change. For larger magnetic fields,  $\omega_c > \omega_o$ , one enters the regimes of the integer and fractional quantum Hall effect. Here, many-body states can arise such as skyrmions or excitations with a fractional charge. On few-electron, vertical quantum dots, some high  $B$ -field experiments have been performed in the integer quantum Hall regime, probing spin flips on decreasing the filling factor from 2 to 1 [18, 19, 50], and the stability of the maximum-density droplet [51]. To date, no clear results have been obtained in the fractional regime.
- (4) *Tunnel coupling between dot and leads.* We have only discussed the regime of weak tunnel coupling; i.e. for tunnel resistances much larger than  $e^2/h = 25 \text{ k}\Omega$ . In this regime the time that an electron spends on the dot is assumed to be much larger than typical relaxation times, implying that the system always returns to equilibrium between consecutive tunnelling events. In addition, the tunnel rate, or lifetime broadening,  $\Gamma$ , has been neglected since in the experiments in this review it has always been much smaller than the thermal energy,  $k_B T$ . Devices have also been made with thinner tunnel barriers so that  $\Gamma \gg k_B T$ . In these devices the Coulomb blockade is no longer complete and higher-order tunnelling processes become visible [52]. Such so-called co-tunnelling events can give rise to the Kondo effect, a many-body effect where many electrons together screen the localized spin on the quantum dot [53]. Under these circumstances quantum dots play a similar role as magnetic impurities in metals, however, again with a much higher degree of experimental control.

The study of transport through few-electron quantum dots was until recently impossible in lateral quantum dots defined by surface gates in a two-dimensional electron gas. However, recently Ciorga *et al* and Gould *et al* [54] realized the few-electron limit in lateral dots. This opens up exciting combinations of experiments on lateral dots (applying high-frequency signals, putting dots in rings, etc [6]) with few-electron regimes where the quantum states are well understood.

## Acknowledgments

The authors would like to thank in particular all the collaborators listed in the periodic table of acknowledgements in figure 2. They further acknowledge the financial support from the Specially Promoted Research, Grant-in-Aid for Scientific Research, from the Ministry of Education, Science and Culture in Japan, from the Dutch Organization for FOM, from the NEDO program NTDP-98, and from the EU via a TMR network.

## References

- [1] See for reviews in popular magazines: Reed M 1993 *Sci. Am.* **268** 118  
Kastner M A 1993 *Phys. Today* **46** 24  
Ashoori R C 1996 *Nature* **379** 413  
Harmans C J P M 1992 *Phys. World* **5** 50  
Kouwenhoven L P and Marcus C M 1998 *Phys. World* **11**
- [2] Alonso M and Finn E J 1968 *Quantum and Statistical Physics* (Reading, MA: Addison-Wesley)
- [3] Austing D G, Honda T, Tokura Y and Tarucha S 1995 *Japan. J. Appl. Phys.* **34** 1320  
Austing D G, Honda T and Tarucha S 1996 *Semicond. Sci. Technol.* **11** 388
- [4] Tarucha S, Austing D G, Honda T, van der Hage R J and Kouwenhoven L P 1996 *Phys. Rev. Lett.* **77** 3613
- [5] Keren K, Stern A and Sivan U 1999 *Preprint cond-mat/9903377*
- [6] See for a review on quantum dots: Kouwenhoven L P, Marcus C M, McEuen P L, Tarucha S, Westervelt R M and Wingreen N S 1997 Electron transport in quantum dots *Mesoscopic Electron Transport* ed L L Sohn, G Schön and L P Kouwenhoven (*Kluwer Series E vol 345*) (June 1996) p 105–214 see also: webpage <http://vortex.tn.tudelft.nl/>
- [7] Marcus C M, Patel S R, Huibers A G, Cronenwett S M, Switkes M, Chan I H, Clarke R M, Folk J A and Godijn S F 1997 *Chaos Solitons Fractals* **8** 1261
- [8] Ralph D C, Black C T, Hergenrother J M, Lu J G and Tinkham M 1997 *Mesoscopic Electron Transport* ed L L Sohn, L P Kouwenhoven and G Schön (*Kluwer Series E vol 345*) (June 1996) p 447–67
- [9] Dekker C 1999 *Phys. Today* **May**
- [10] Grabert H and Devoret M H (ed) 1991 *Single Charge Tunnelling* (New York: Plenum)  
Jacak L, Harylak P and Wojs A 1998 *Quantum Dots* (Berlin: Springer)
- [11] Iafate G J, Hess K, Krieger J B and Macucci M 1995 *Phys. Rev. B* **52** 10737
- [12] Hadley P and Mooij J E 2000 *Quantum Semiconductor Devices and Technologies* ed T P Pearsall (Dordrecht: Kluwer)
- [13] Mizuto H and Tanoue T 1996 *The Physics and Applications of Resonant Tunnelling Diodes* (Cambridge: Cambridge University Press)
- [14] Tokura Y 1999 Private communication
- [15] Su B, Goldman V J and Cunningham J E 1992 *Phys. Rev. B* **46** 7644  
Tewordt M, Martín-Moreno L, Law V J, Kelly M J, Newbury R, Pepper M, Ritchie D A, Frost J E F and Jones G A C 1992 *Phys. Rev. B* **46** 3948  
Schmidt T, Tewordt M, Blick R H, Haug R J, Pfannkuche D, von Klitzing K, Förster A and Lüth H 1995 *Phys. Rev. B* **51** 5570
- [16] Dellow M W, Beton P H, Langerak C J G M, Foster T J, Main P C, Eaves L, Henini M, Beaumont S P and Wilkinson C D W 1992 *Phys. Rev. Lett.* **68** 1754  
Gueret P, Blanc N, Germann R and Rothuizen H 1992 *Phys. Rev. Lett.* **68** 1896
- [17] Tarucha S, Austing D G and Honda T 1995 *Superlatt. Microstruct.* **18** 121
- [18] Ashoori R C, Störmer H L, Weiner J S, Pfeiffer L N, Pearton S J, Baldwin K W and West K W 1992 *Phys. Rev. Lett.* **68** 3088
- [19] Ashoori R C, Störmer H L, Weiner J S, Pfeiffer L N, Baldwin K W and West K W 1993 *Phys. Rev. Lett.* **71** 613
- [20] Korotkov A N, Averin D V and Likharev K K 1990 *Physica B* **165/166** 927  
Beenakker C W J 1991 *Phys. Rev. B* **44** 1646  
Averin D V, Korotkov A N and Likharev K K 1991 *Phys. Rev. B* **44** 6199
- [21] Fock V 1928 *Z. Phys.* **47** 446  
Darwin C G 1930 *Proc. Camb. Phil. Soc.* **27** 86
- [22] Halonen V, Hyvonen P, Pietilinen P and Chakraborty T 1996 *Phys. Rev. B* **53** 6971
- [23] Macucci M, Hess K and Iafate G J 1993 *Phys. Rev. B* **48** 17354  
Macucci M, Hess K and Iafate G J 1995 *J. Appl. Phys.* **77** 3267

- [24] Zeng Y H, Goodman B and Serota R A 1993 *Phys. Rev. B* **47** 15660
- [25] Rontani M, Rossi F, Manghi F and Molinari E 1997 *Appl. Phys. Lett.* **72** 975  
Rontani M, Rossi F, Manghi F and Molinari E 1999 *Phys. Rev. B* **59** 10165
- [26] Warburton R J, Miller B T, Dürr C S, Bödefeld C, Karrai K, Kotthaus J P, Medeiros-Ribeiro G and Petroff P M 1998 *Phys. Rev. B* **58** 16221
- [27] Tarucha S, Austing D G, Tokura Y, van der Wiel W G and Kouwenhoven L P 2000 *Phys. Rev. Lett.* **84** 2485
- [28] Stopa M 1996 *Phys. Rev. B* **54** 13767
- [29] Stewart D R, Sprinzak D, Marcus C M, Duruöz C I and Harris J S 1997 *Science* **278** 1784
- [30] Heiss W D and Nazmitdinov R G 1996 *Phys. Lett. A* **222** 309
- [31] Ezaki T, Mori N and Hamaguchi C 1997 *Phys. Rev. B* **56** 6428
- [32] Angelucci A and Tagliacozzo A 1997 *Phys. Rev. B* **56** 7088
- [33] Nagaraja S, Matagne P, Thean V-Y, Leburton J-P, Kim Y-H and Martin R M 1997 *Phys. Rev. B* **56** 15752
- [34] Steffens O, Rössler U and Suhrke M 1998 *Europhys. Lett.* **42** 529
- [35] Lee I-H, Rao V, Martin R M and Leburton J-P 1998 *Phys. Rev. B* **57** 9035
- [36] Harting J, Müllen O and Borrmann P 2000 *Phys. Rev. B* **62** 10207–11
- [37] Wojs A and Hawrylak P 1996 *Phys. Rev. B* **53** 10841
- [38] See, for example, Kumar A, Laux S E and Stern F 1990 *Phys. Rev. B* **42** 5166–75  
Hallam L D, Weis J and Maksym P A 1996 *Phys. Rev. B* **53** 1452
- [39] Bednarek S, Szafran B and Adamowski J 2000 *Phys. Rev. B* **61** 4461
- [40] Wagner M, Merkt U and Chaplik A V 1992 *Phys. Rev. B* **45** 1951
- [41] Thurner G, Herold H, Ruder H, Schlicht G and Wunner G 1982 *Phys. Lett. A* **89** 133
- [42] Ashoori R C, Stormer H L, Weiner J S, Pfeiffer L N, Baldwin K W and West K W 1993 *Phys. Rev. Lett.* **71** 613
- [43] Kouwenhoven L P, Oosterkamp T H, Danoesastro M W S, Eto M, Austing D G, Honda T and Tarucha S 1997 *Science* **278** 1788
- [44] van der Wiel W G, Oosterkamp T H, Janssen J W, Kouwenhoven L P, Austing D G, Honda T and Tarucha S 1998 *Physica B* **256–8** 173
- [45] Eto M 1997 *Japan. J. Appl. Phys.* **36** 3924
- [46] Natori A *et al* 1997 *Japan. J. Appl. Phys.* **36** 3960  
Tamura H 1998 *Physica B* **249–51** 210  
Hirose K and Wingreen N S 1999 *Phys. Rev. B* **59** 4604–7
- [47] Koskinen M, Manninen M and Reimann S M 1997 *Phys. Rev. Lett.* **79** 1817
- [48] See also our review that includes a discussion on the effects of symmetry-breaking in non-circular quantum dots:  
Tarucha S, Austing D G, Sasaki S, Tokura Y, van der Wiel W G and Kouwenhoven L P 2000 *Appl. Phys. A* **71** 367–78
- [49] Bryant G W 1987 *Phys. Rev. Lett.* **59** 1140  
Hausler W, Kramer B and Masek J 1991 *Z. Phys. B* **85** 435  
Maksym P A 1993 *Physica B* **184** 385  
Bedanov V M and Peeters F M 1994 *Phys. Rev. B* **49** 2667  
Koulakov A A and Sklovskii B I 1998 *Phys. Rev. B* **57** 2352–67
- [50] Austing D G, Tokura Y, Honda T, Tarucha S, Danoesastro M, Janssen J W, Oosterkamp T H and Kouwenhoven L P 1999 *Japan. J. Appl. Phys.* **38** 372–5
- [51] Oosterkamp T H, Janssen J W, Kouwenhoven L P, Austing D G, Honda T and Tarucha S 1999 *Phys. Rev. Lett.* **82** 2931–4
- [52] De Franceschi S, Sasaki S, Elzerman J M, van der Wiel W G, Tarucha S and Kouwenhoven L P 2001 *Phys. Rev. Lett.* **86** 878–81
- [53] Sasaki S, De Franceschi S, Elzerman J M, van der Wiel W G, Eto M, Tarucha S and Kouwenhoven L P 2000 *Nature* **405** 764–7
- [54] Ciorga M, Sachrajda A S, Hawrylak P, Gould C, Zawadzki P, Jullian S, Feng Y and Wasilewski Z 2000 *Phys. Rev. B* **61** R16315–8  
Gould C, Hawrylak P, Sachrajda A, Feng Y, Zawadzki P and Wasilewski Z 2000 *Physica E* **6** 461–5